



# High Order Finite Volume Schemes for Solving the Non-Conservative Convection Equations on the Unstructured Grids

Qian-Min Huang<sup>1</sup> · Yu-Xin Ren<sup>1</sup> · Qian Wang<sup>2</sup>

Received: 30 March 2020 / Revised: 9 April 2021 / Accepted: 25 May 2021 /

Published online: 24 June 2021

© The Author(s), under exclusive licence to Springer Science+Business Media, LLC, part of Springer Nature 2021

## Abstract

In this paper, a high order finite volume scheme for solving the non-conservative convection equations on the unstructured grids is proposed. It is found that when the non-conservative convection equations are rewritten into the conservative form with additional source term, the direct application of the finite volume scheme using high order reconstruction will produce numerical instability. To solve this problem, we propose in the present paper to solve the integral form of the non-conservative convection equations. To account for the upwinding effect, a convective reconstruction technique is proposed. The proposed method is applied to solve a linear advection equation and the eikonal equation in time dependent non-conservative form. An artificial viscosity term is added to handle the singularity of the equation. The numerical results show that the proposed numerical scheme can achieve high order accuracy and is very robust.

**Keywords** Non-conservative convection equation · Eikonal equation · Variational reconstruction · Convective reconstruction

## 1 Introduction

In a series of recent papers [1–5], several compact reconstruction techniques have been proposed within the framework of the high order finite volume (FV) schemes on the unstructured grids. One distinctive advantage of these methods is that they can be applied based on a compact data structure involving only the central control volume and its direct neighbors (the von Neumann neighbors). It is in this point, the proposed schemes are similar to other compact stencil high order schemes on the unstructured grids including the discontinuous Galerkin (DG) [6–8], flux reconstruction (FR) [9–11], PnPm [12], hybrid DG/FV [13, 14], multi-moment [15–17], and compact gas-kinetic schemes [18, 19]. Among the compact

---

✉ Yu-Xin Ren  
ryx@tsinghua.edu.cn

<sup>1</sup> Department of Engineering Mechanics, Tsinghua University, Beijing 100084, China

<sup>2</sup> Mathematics Section, Ecole Polytechnique Fédérale de Lausanne, CH-1015 Lausanne, Switzerland

reconstruction techniques proposed, the variational reconstruction (VR) has shown promising potentials since it is accurate, robust and non-singular [3]. It has been used in the hybrid DG/FV schemes and rDG schemes as the reconstruction procedure [20–24].

In the present paper, we will study the numerical procedure for solving the non-conservative convection equations using the high order compact FV scheme based on the VR. Specifically, a linear advection equation in non-conservative form and the eikonal equation in time-dependent form are used as the examples. Since the numerical methods for solving the linear advection equation are well known, here the numerical methods for solving the eikonal equation will be briefly reviewed. The eikonal equation is a first-order hyperbolic partial differential equation. It has been seen in many fields such as geometric optics, computational geometry, computational fluid dynamics (CFD), computational vision, material science, and optimal control [25]. Eikonal equation takes the form of

$$\begin{cases} |\nabla \phi| = f, \\ \phi|_{\Gamma} = 0, \end{cases} \quad (1)$$

where  $\phi = \phi(\vec{x})$  with  $\vec{x} \in \Omega \subset \mathbf{R}^n$ ,  $\Gamma = \partial\Omega$  is the boundary of the domain, and  $f = f(\vec{x})$  is a positive propagation function. Generally speaking, the numerical method for eikonal equation can be divided into two categories: one is to solve a steady-state boundary value problem [26, 27], the other is to solve a time-dependent problem by introducing a pseudo time derivative term [38–40]. And the latter is the form solved in the present paper.

The methods for solving the steady-state boundary value problem mainly include the fast marching method (FMM) and the fast sweeping method (FSM). FMM uses upwind difference scheme to discretize eikonal equation. Conventionally, heap sorting is adopted in FMM to avoid iterations in the solving process. The computational complexity of FMM is about  $O(N \log N)$ , where  $N$  is the grid number. Unlike FMM, FSM uses the Gauss–Seidel iterations with alternating scanning sequence to solve the equation discretized by the nonlinear upwind difference scheme. The computational complexity of FSM is about  $O(N)$ . The convergence speed of FSM for the problems with simple geometry is faster than that of FMM, but for problems with non-uniformity or complex geometry, the opposite results may appear. To realize high order FSM or FMM, ENO/WENO [27–30] or DG [31–34] have been used. Furthermore, parallel algorithms for FSM and FMM have also been proposed to solve the large scale problems [35–37].

The time-dependent eikonal equation is obtained by the introduction of a pseudo time derivative term into the square of the eikonal equation. To derive this equation, Eq. (1) is reformulated as

$$\nabla \phi \cdot \nabla \phi = f^2.$$

Then a pseudo time derivative is added to the above equation, and the pseudo convective velocity vector is defined by

$$\vec{u} = \nabla \phi.$$

The resulting equation is therefore

$$\frac{\partial \phi}{\partial \tau} + \vec{u} \cdot \nabla \phi = f^2. \quad (2)$$

Equation (2) is a first order hyperbolic equation with a source term. In the form of Eq. (2), the eikonal equation is a non-conservative convection equation. The advantages of the

time dependent form are twofold. On one hand, high order discretization can be realized easily by applying the existing high order schemes for the time dependent problems. On the other hand, large scale parallel computations can be straightforwardly implemented by using the domain decomposition method. Previous studies of the time-dependent eikonal equation have been focused on the minimum wall distance computation [38–41]. Various spatial discretization schemes have been applied to solve Eq. (2), including the finite difference [38], DG [39, 40], and FV [41–48] schemes. In the present paper, we will solve Eq. (2) using the high order FV schemes based on the compact VR.

In the FV schemes, the integral form of Eq. (2) is numerically solved. The direct integration of Eq.(2) over control volume  $\Omega_i$  leads to

$$\frac{\partial \bar{\phi}}{\partial \tau} + \frac{1}{\Omega_i} \iint_{\Omega_i} \vec{u} \cdot \nabla \phi d\Omega = \frac{1}{\Omega_i} \iint_{\Omega_i} f^2 d\Omega , \quad (3)$$

where  $\bar{\phi}$  is the cell average of  $\phi$  on cell  $\Omega_i$ . In the present paper, Eq.(3) is called the integral form of non-conservative equation (NCE). In traditional FV methods, to introduce the upwind discretization technique, the integration of the convection term is written as the summation of a conservative term and an integral source term, and the governing equation becomes

$$\frac{\partial \bar{\phi}}{\partial \tau} + \frac{1}{\Omega_i} \oint_{\partial \Omega_i} \phi \vec{u} \cdot \vec{n} dS = \frac{1}{\Omega_i} \iint_{\Omega_i} (\phi \Delta \phi + f^2) d\Omega . \quad (4)$$

In the present paper, Eq. (4) is called the integral form of quasi-conservative equation (QCE). On the left hand side of Eq. (4), the second term is the conservative term and source term is at the right hand side. The numerical flux of the conservative term is usually computed by a certain Riemann solver or flux splitting technique, while the source term is computed in terms of the reconstructed distribution of the dependent variable  $\phi$  from its cell average values within the reconstruction stencil. Numerical instabilities have been reported when solving this form of governing equation. Xia and Tucker have used the first-order FV methods to solve the quasi-conservative eikonal equation on triangular elements. They adopted velocity and Laplacian clipping and velocity under-relaxation to overcome the numerical instability [41]. Zhou and Wang have used DG methods to solve this problem on quadrilateral element. They froze the convective velocity and modified Laplacian in the frozen period to improve the stability [39]. Stefan and Ralf have used DG methods to solve the quasi-conservative eikonal equation on quadrilateral element. They adopted the streamline diffusion method to improve the stability [40].

When using the high order FV scheme based on the VR to solve Eq. (4), the numerical instability is also observed. Figure 1 shows the numerical results during the simulation computed using the fourth order FV scheme based on the VR, in which the numerical oscillations can be clearly observed. These oscillations will further develop and sometimes lead to blow up of the numerical solution.

Because of the non-conservative nature of the problem, it is necessary to study the numerical methods solving NCE directly. In fact, a number of finite volume methods have been developed to solve the hyperbolic NCE and conservation laws with non-conservative products [42–46] based on weak solutions of nonconservative hyperbolic PDE defined in [47]. In the present paper, a new high order finite volume scheme on the unstructured grids will be proposed for solving hyperbolic NCE by introducing the upwind property into the reconstruction procedure.

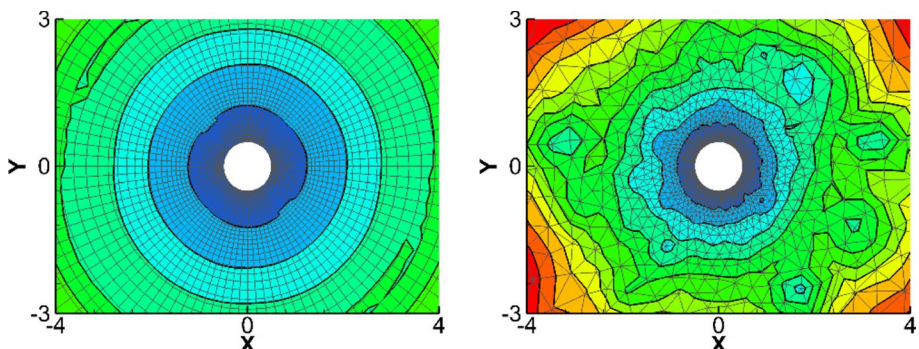


**Fig. 1** Numerical instability when solving Eq.(3) ( $f = 1$ ) using the fourth order compact FV scheme based on the VR

To solve Eq. (3) using the high order scheme, the VR [3] is used to reconstruct the polynomial distribution of the solution in each control volume from the cell averages of the solution. In the discretization of the convection term of the integral form of NCE shown in Eq. (3), an important problem is how should the upwinding effect be introduced. In the present paper, the solution to this problem is to propose another reconstruction called the convective reconstruction (CR). The details of the CR will be presented in Sect. 2.2. In Sect. 3, an analysis in terms of the second order FV scheme solving Burgers equation shows that, by using the CR, proper numerical dissipation can be introduced to stabilize the numerical scheme. The analysis also indicates that negative dissipation will probably be presented if QCE or Eq. (4) is solved using the conventional FV scheme. These analyses confirm the importance of using NCE and CR.

It is well-known that the local singularity (discontinuity in the derivatives) will be presented in solution of the eikonal equation due to its non-linear and hyperbolic nature. To solve this problem, an artificial viscosity (AV) term is introduced in the governing equation. Numerical experiments show that the singularity can be effectively overcome without using additional limiter when the coefficient of AV is properly chosen. Meanwhile, the introduction of the numerical viscosity will not affect the accuracy of the numerical scheme. The AV for handing the discontinuities is also proposed and tested in solving the linear advection equation with discontinuous initial conditions.

We should notice here that the numerical schemes presented in this paper can be also applied to other non-conservative equations although only the linear advection equation and the eikonal equation are studied. The rest of this paper is organized as follows. The high order FV scheme for solving the non-conservative convective equation and the CR are introduced in Sect. 2. The analysis of the effect of the CR is presented in Sect. 3. The numerical results are discussed in Sect. 4. And the conclusions are given in Sect. 5.

## 2 Numerical Methods

### 2.1 High Order Finite Volume Scheme for Solving the Non-Conservative Convective Equation

For the present FV scheme, the computational domain  $\Omega$  is partitioned into  $N$  non-overlapping control volumes, i.e.,  $\Omega = \bigcup_{i=1}^N \Omega_i$ , where  $\Omega_i$  is used to denote the  $i$ -th control volume. And the volume of  $\Omega_i$  is denoted as  $\bar{\Omega}_i$ . The governing equation solved in the present paper is the following integral form of NCE,

$$\frac{\partial \bar{\phi}}{\partial \tau} + \frac{1}{\bar{\Omega}_i} \iint_{\Omega_i} \vec{u} \cdot \nabla \phi d\Omega = \frac{1}{\bar{\Omega}_i} \iint_{\Omega_i} s d\Omega , \quad (5)$$

where

$$\bar{\phi}_i = \frac{1}{\bar{\Omega}_i} \iint_{\Omega_i} \phi(\vec{x}, \tau) d\Omega ,$$

is the cell average of solution  $\phi(\vec{x}, \tau)$  on the control volume  $\Omega_i$ . Eq. (5) is the linear advection equation if  $s = 0$  and  $\vec{u}$  is independent of  $\phi$ , and is the eikonal equation if  $s = f^2$  and the velocity vector is defined by

$$\vec{u} = \nabla \phi .$$

For the eikonal equation, when  $f = 1$ , the dependent variable  $\phi$  is the nearest distance to the wall boundary. Therefore, at the wall boundary, the boundary value is  $\phi = 0$ . At the far-field boundary, no boundary condition needs to be specified.

A straightforward numerical procedure to solve Eq. (5) is to reconstruct the polynomial function of  $\phi$  from its cell averages, and then use the reconstructed function to compute the convection term  $\iint_{\Omega_i} \vec{u} \cdot \nabla \phi d\Omega$  in Eq. (5) directly. However, the problems will arise in that the evaluation of the convection term fails to consider the wave propagation or upwinding effect, which is usually required to stabilize the numerical schemes. To solve this problem, we propose the CR, which is conducted based on the results of the VR and a state Riemann solver to realize the upwinding effect. Both CR and VR are applied in the evaluation of the non-conservative convective term in Eq. (5).

### 2.2 Variational Reconstruction

The proposed CR is based on VR proposed in [3]. Therefore, the VR is briefly reviewed here. For VR of any order of accuracy, the reconstruction is implemented on a compact stencil only involving the current and its face-neighboring control volumes. For the internal cell  $\Omega_i$  of the 2D computational domain, the stencil is  $S_i = \{\Omega_i, \Omega_{j1}, \Omega_{j2}, \Omega_{j3}\}$ , and for the boundary cell, the stencil is  $S_i = \{\Omega_i, \Omega_{j1}, \Omega_{j2}\}$ , as shown in Fig. 2.

Let the degree  $k$  reconstruction polynomial of the solution  $\phi(\vec{x})$  on control volume  $\Omega_i$  be

$$\phi_i(\vec{x}) = \bar{\phi}_i + \sum_{l=1}^{N_c(k)} \phi_{i,l} \psi_{i,l}(\vec{x}) , \quad (6)$$

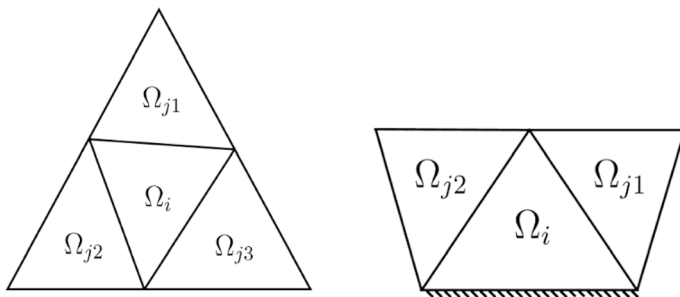


**Fig. 2** Stencil for control volume  $\Omega_i$ , internal cell (left) and boundary cell (right)

where  $\phi_{i,l}$  is the coefficients to be determined in the reconstruction,  $N_c(k) = (k+1)(k+2)/2 - 1$  is the number of the unknown coefficients, and  $\psi_{i,l}(\vec{x})$  is the zero-mean basis defined by

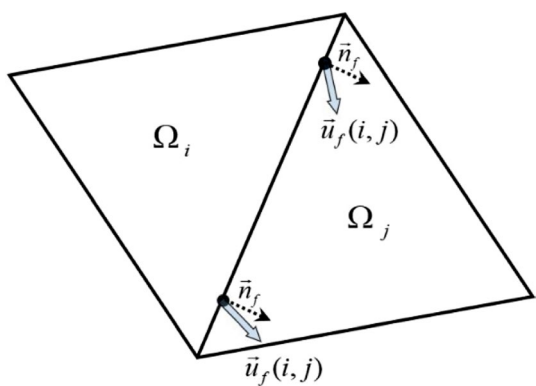
$$\begin{aligned}\psi_{i,l}(\vec{x}) &= \delta x_i^p \delta x_i^q - \overline{\delta x_i^p \delta x_i^q}, \\ \delta x_i &= \frac{x - x_i}{\Delta x_i}, \quad \delta y_i = \frac{y - y_i}{\Delta y_i}, \\ \overline{\delta x_i^p \delta x_i^q} &= \frac{1}{\Omega_i} \iint_{\Omega_i} \delta x_i^p \delta x_i^q d\Omega.\end{aligned}$$

In above equations,  $p$  and  $q$  are the powers of the corresponding Taylor basis. The length scale  $\Delta x$  and  $\Delta y$  are defined following the proposal of Luo et al. [49]

$\Delta x_i = \frac{x_{i,\max} - x_{i,\min}}{2}$ ,  $\Delta y_i = \frac{y_{i,\max} - y_{i,\min}}{2}$ , where  $x_{i,\max}$ ,  $x_{i,\min}$  and  $y_{i,\max}$ ,  $y_{i,\min}$  are respectively the maximum and minimum  $x$ -and  $y$ -coordinates of the control volume (Fig. 3).

In the variational reconstruction procedure, the linear equation system to determine the unknown coefficients of the reconstruction polynomials is derived by minimizing the cost function using the direct variational method. The specific reconstruction depends on the form of the cost function. In Ref. [3], the cost function is taken as the interface jump integration (IJI), which is a measure of the jump of the reconstructed polynomial and its derivatives at the interface or edge of the control volume. In the present paper, the specific IJI for each internal edge of the computational domain is defined by

**Fig. 3** The conceptual figure of Eq. (15) for control volume  $\Omega_i$ , where the dots are located at the Gaussian points



$$I_f(i,j) = \frac{1}{|S_{ij}|} \int_f \sum_{p=0,q=0}^{p+q \leq k} \left[ \Delta x_{ij}^p \Delta y_{ij}^q \frac{C_{p+q}^p}{(p+q)!} \left( \frac{\partial^{p+q} \phi_i(\vec{x})}{\partial x^p \partial y^q} - \frac{\partial^{p+q} \phi_j(\vec{x})}{\partial x^p \partial y^q} \right) \right]^2 ds, \quad (7)$$

where the subscript “ $f$ ” stands for the edge or interface shared by control volumes  $\Omega_i$  and  $\Omega_j$ , i.e.  $f = \partial\Omega_i \cap \partial\Omega_j$ ,  $|S_{ij}|$  is the length of the interface, and  $\Delta x_{ij} = \frac{1}{2}(\Delta x_i + \Delta x_j)$  and  $\Delta y_{ij} = \frac{1}{2}(\Delta y_i + \Delta y_j)$ . IJI for the boundary edge of the computational domain is defined by

$$I_{bf}(i) = \frac{1}{|S_{bf}|} \int_{bf} [\phi_i(\vec{x}) - \phi_{bf}(\vec{x})]^2 ds, \quad (8)$$

where the subscript “ $bf$ ” stands for the boundary edge of cell  $\Omega_i$ , and  $|S_{bf}|$  is the length of the boundary edge. In Eq. (8),  $\phi_{bf}(\vec{x})$  is the boundary value of  $\phi(\vec{x})$  which will be discussed further later in this section.

The cost function takes the summation of all IJIs of the computational domain, i.e.,

$$I = \sum_{f=1}^{N_f} I_f(i,j) + \sum_{bf=1}^{N_{bf}} I_{bf}(i), \quad (9)$$

where  $N_f$  denotes the number of internal edges of the control volumes, and  $N_{bf}$  denotes the number of boundary edges where physical boundaries are located. The constitutive relations of VR can be established by minimizing the cost function of Eq. (9), namely

$$\frac{\partial I}{\partial \phi_{i,l}} = 0, \quad l = 1, 2, \dots, N_c(k), \quad i = 1, 2, \dots, N. \quad (10)$$

According to Fig. 2, the unknown coefficients of the reconstructed polynomial  $\phi_{i,l}$  on control volume  $\Omega_i$  are related directly only to the information defined on the stencil  $S_i$ . By substituting Eq. (6) into Equations (7)–(10), the following linear equations can be derived

$$\begin{aligned} & \sum_{l=1}^{N_c(k)} \left\{ \left[ \sum_{j \in S_i, j \neq i} \frac{1}{|S_{ij}|} \int_{\partial\Omega_i \cap \partial\Omega_j} \sum_{p=0,q=0}^{p+q \leq k} \Delta x_{ij}^{2p} \Delta y_{ij}^{2q} \frac{C_{p+q}^p}{(p+q)!^2} \frac{\partial^{p+q} \psi_{i,l}}{\partial x^p \partial y^q} \frac{\partial^{p+q} \psi_{i,r}}{\partial x^p \partial y^q} ds \right] \right. \\ & \quad \left. + \delta_{bf} \frac{1}{|S_{bf}|} \int_{bf} \psi_{i,l} \psi_{i,r} ds \right\} \phi_{i,l} \\ &= \sum_{j \in S_i, j \neq i} \left\{ \sum_{l=1}^{N_c(k)} \left[ \frac{1}{|S_{ij}|} \int_{\partial\Omega_i \cap \partial\Omega_j} \sum_{p=0,q=0}^{p+q \leq k} \Delta x_{ij}^{2p} a \Delta y_{ij}^{2q} \frac{C_{p+q}^p}{(p+q)!^2} \frac{\partial^{p+q} \psi_{i,l}}{\partial x^p \partial y^q} \frac{\partial^{p+q} \psi_{j,r}}{\partial x^p \partial y^q} ds \right] \phi_{j,l} \right\} \\ & \quad + \sum_{j \in S_i, j \neq i} \int_{\partial\Omega_i \cap \partial\Omega_j} \frac{\psi_{i,r}}{|S_{ij}|} (\bar{\phi}_j - \bar{\phi}_i) ds + \delta_{bf} \int_{bf} \frac{\psi_{i,r}}{|S_{bf}|} (\phi_{bf} - \bar{\phi}_i) ds, \\ & l = 1, 2, \dots, N_c(k), \quad r = 1, 2, \dots, N_c(k), \end{aligned} \quad (11)$$

where parameter  $\delta_{bf}$  takes the form

$$\begin{cases} \delta_{bf} = 0, & \Omega_i \text{ is inner control volume} \\ \delta_{bf} = 1, & \Omega_i \text{ is boundary control volume} \end{cases}$$

Equation (11) can be arranged into the matrix form

$$\mathbf{A}_i \vec{\phi}_i = \sum_{j \in S_i, j \neq i} \mathbf{A}_j \vec{\phi}_j + \vec{b}_i \quad (12)$$

with

$$\begin{aligned} \mathbf{A}_i = & \left[ \sum_{j \in S_i, j \neq i} \frac{1}{|S_{ij}|} \int_{\partial\Omega_i \cap \partial\Omega_j} \Delta x_{ij}^{2p} \Delta y_{ij}^{2q} \frac{C_{p+q}^{p^2}}{(p+q)!^2} \frac{\partial^{p+q} \psi_{i,l}}{\partial x^p \partial y^q} \frac{\partial^{p+q} \psi_{i,r}}{\partial x^p \partial y^q} ds \right] \\ & + \delta_{bf} \frac{1}{|S_{bf}|} \int_{bf} b_f \psi_{i,l} \psi_{i,r} ds, \end{aligned}$$

$$\mathbf{A}_j = \left[ \frac{1}{|S_{ij}|} \int_{\partial\Omega_i \cap \partial\Omega_j} \Delta x_{ij}^{2p} \Delta y_{ij}^{2q} \frac{C_{p+q}^{p^2}}{(p+q)!^2} \frac{\partial^{p+q} \psi_{i,l}}{\partial x^p \partial y^q} \frac{\partial^{p+q} \psi_{j,r}}{\partial x^p \partial y^q} ds \right]$$

$$\vec{\phi}_i = [\phi_{i,1}, \phi_{i,2}, \dots, \phi_{i,N_c(k)}]^T,$$

$$\vec{b}_i = \sum_{j \in S_i, j \neq i} \int_{\partial\Omega_i \cap \partial\Omega_j} \frac{\psi_{i,r}}{|S_{ij}|} (\bar{\phi}_j - \bar{\phi}_i) ds + \delta_{bf} \int_{bf} \frac{\psi_{i,r}}{|S_{bf}|} (\phi_{bf} - \bar{\phi}_i) ds,$$

$\mathbf{A}_i$  and  $\mathbf{A}_j$  are numerically computed using Gaussian quadrature rule. They are geometrical quantities that are computed only once and stored for future use. Assembling the reconstruction relationships, Eq. (12), of all control volumes into the global matrices, we have

$$\mathbf{A} \vec{\phi} = \vec{b}, \quad (13)$$

where

$$\begin{aligned} \mathbf{A} &= \mathbf{D} - \mathbf{L} - \mathbf{U}, \quad \mathbf{D} = \{\mathbf{A}_i\}, \quad \mathbf{L} = \{\mathbf{A}_j, j < i\}, \\ \mathbf{U} &= \{\mathbf{A}_j, j > i\}, \quad \vec{\phi} = \{\vec{\phi}_i\}, \quad \vec{b} = \{\vec{b}_i\}. \end{aligned}$$

It can be proved that the coefficient matrix  $\mathbf{A}$  established by the above method is symmetric and positive definite and  $2\mathbf{D} - \mathbf{A}$  is also positive definite. These properties guarantee the existence of unique solutions for the system (13), and the convergence of some well-known iteration solvers. This is an important advantage of VR over the compact least squares [2] and the k-exact [50] schemes. In practice, Eqs. (12) or (13) is solved by using the block Gauss–Seidel iteration, i.e.

$$\vec{\phi}_i^{(m+1)} = \mathbf{A}_i^+ \left( \sum_{j \in S_i, j > i} \mathbf{A}_j \vec{\phi}_j^{(m+1)} + \sum_{j \in S_i, j > i} \mathbf{A}_j \vec{\phi}_j^{(m)} \right) + \mathbf{A}_i^+ \vec{b}_i^{(m)}. \quad (14)$$

It is worth noting that when implementing the iterative solver, only the information of current and face-neighboring cells is required. Therefore, only the data structures defined in terms of a compact stencil need to be maintained. To improve the efficiency of the proposed numerical scheme, the iteration is coupled with the iteration used in time integration scheme. This approach guarantees the execution efficiency of VR, which has been discussed in Ref. [3]. In the present paper, the steady state solution of the eikonal equation is computed by solving a

time-dependent problem. According to the solution procedure proposed in [3], the iteration of Eq. (14) is performed once in every step of the time advancement. For each element, the Moore–Penrose inverse is used in the iteration procedure as shown in Eq. (14). Since the coefficient matrix is solution independent, its Moore–Penrose inverse is calculated in the initialization stage and stored, which can further reduce the computational costs.

We notice that in this procedure the boundary conditions have been considered through Eq. (8). For the Dirichlet boundary condition,  $\phi_{bf}$  is chosen as the known boundary value so that the difference between  $\phi_i$  and  $\phi_{bf}$  at the boundary will be minimized by using Eq. (10). For the far field boundary,  $\phi_{bf}$  is computed by the local reconstruction of the previous iteration. In this case, Equations (8)~(12) introduce a certain relaxation in the iteration procedure of Eq. (14).

### 2.3 Convective Reconstruction

After this brief review of the VR, we now present the details of CR, which is newly proposed in the present paper to account for the upwinding effect in the FV schemes solving the integral form of NCE.

The basic idea of CR is to compute the dependent variable at the cell interface using VR and a state Riemann solver to account for the upwinding effect, and then to reconstruct the distribution of the dependent variable within the cell using the interfacial values of the dependent variable. Therefore, the CR is implemented in terms of a two-step procedure. In the first step, the dependent variable at the interface of the control volume is computed using a state Riemann solver of which the left and right states are computed in terms of the existing VR. To be specific, at the interface shared by  $\Omega_i$  and  $\Omega_j$ , the interfacial value of  $\phi_f(i,j)$  is

$$\begin{aligned}\phi_f(i,j) &= \frac{1}{2}[1 + \text{sign}(\vec{u}_f(i,j) \cdot \vec{n}_f)]\phi_i(\vec{x}_f) + \frac{1}{2}[1 - \text{sign}(\vec{u}_f(i,j) \cdot \vec{n}_f)]\phi_j(\vec{x}_f), \\ \vec{u}_f(i,j) &= \frac{1}{2}(\nabla\phi_i(\vec{x}_f) + \nabla\phi_j(\vec{x}_f)),\end{aligned}\quad (15)$$

where  $\phi_i(\vec{x}_f)$  and  $\phi_j(\vec{x}_f)$  are computed using the results of VR. The upwinding or wave propagation effect is accounted for by sign of  $\vec{u}_f(i,j) \cdot \vec{n}_f$ . In the second step, a polynomial function is reconstructed on the control volume using function approximation technique from the interfacial value obtained in the first step. Let the approximate polynomials of CR on the control volume  $\Omega_i$  be as follows

$$\tilde{\phi}_i(\vec{x}) = \bar{\phi}_i + \sum_{l=1}^{N_c(k)} \tilde{\phi}_{i,l} \psi_{i,l}(\vec{x}),$$

where the mean values  $\bar{\phi}_i$  and basis functions  $\psi_{i,l}(\vec{x})$  are the same as VR. It is worth to note that the degree of the polynomial of the CR is chosen to be identical to the polynomial of VR. The unknowns in  $\tilde{\phi}_i(\vec{x})$  are determined by minimizing the following cost function

$$\tilde{I}_f(i) = \sum_{j \in S_i, j \neq i} \int_f (\tilde{\phi}_i(\vec{x}_f) - \phi_f(i,j))^2 ds,$$

where  $\phi_f(i,j)$  is computed using Eq. (15). Using

$$\frac{\partial \tilde{I}}{\partial \tilde{\phi}_{i,l}} = 0, \quad l = 1, 2, \dots, N_c(k), \quad i = 1, 2, \dots, N$$

the linear equations are derived as

$$\begin{aligned} & \sum_{l=1}^{N_c(k)} \left( \sum_{j \in S_i, j \neq i} \int_{\partial\Omega_i \cap \partial\Omega_j} \psi_{i,l} \psi_{i,r} ds + \delta_{bf} \int_{bf} \psi_{i,l} \psi_{i,r} ds \right) \tilde{\phi}_{i,l} \\ &= \sum_{j \in S_i, j \neq i} \int_{\partial\Omega_i \cap \partial\Omega_j} (\phi_{f,j} - \bar{\phi}_i) \psi_{i,r} ds + \delta_{bf} \int_{bf} \psi_{i,r} (\phi_{bf} - \bar{\phi}_i) ds, \\ & r = 1, 2, \dots, N. \end{aligned} \quad (16)$$

Equation (16) can be arranged into the matrix form

$$\tilde{\mathbf{A}}_i \vec{\tilde{\phi}}_i = \vec{\tilde{b}}_i, \quad (17)$$

with

$$\begin{aligned} \tilde{\mathbf{A}}_i &= \sum_{j \in S_i, j \neq i} \int_{\partial\Omega_i \cap \partial\Omega_j} \psi_{i,l} \psi_{i,r} ds + \delta_{bf} \int_{bf} \psi_{i,l} \psi_{i,r} ds \quad \vec{\tilde{\phi}}_i = [\tilde{\phi}_{i,1}, \tilde{\phi}_{i,2}, \dots, \tilde{\phi}_{i,N_c(k)}]^T, \\ \vec{\tilde{b}}_i &= \sum_{j \in S_i, j \neq i} \int_{\partial\Omega_i \cap \partial\Omega_j} (\phi_{f,j} - \bar{\phi}_i) \psi_{i,r} ds + \delta_{bf} \int_{bf} \psi_{i,r} (\phi_{bf} - \bar{\phi}_i) ds, \end{aligned}$$

Equations (16) or (17) is solved to obtain  $\tilde{\phi}_{i,l}$ . We notice that CR can be solved locally without the need to solve a globally coupled system of equations.

The VR and CR give two sets of reconstruction polynomials on each control volume. If the convective velocity is given, we only need to calculate the quantity being transported, i.e.  $\nabla\phi$ , via the CR. Otherwise, to compute  $\iint_{\Omega_i} \vec{u} \cdot \nabla\phi d\Omega$  in Eq. (5), we have several choices, as shown in Table 1.

Scheme 1 is the method that we have tested initially. As having been discussed in the beginning of this section, it fails to account for the wave propagation effect. Numerical tests show that numerical instability occurs during the simulations. In scheme 2, the convective velocity  $\vec{u}$  is computed using VR which is basically a central scheme with respect to the cell center, and  $\nabla\phi$ , the quantity being transported, is computed using CR. Numerical results show that scheme 2 predicts numerical results slightly better than scheme 3, in which both terms are computed using CR. Therefore, in the following sections, only scheme 2 is used.

## 2.4 Artificial Viscosity

### 2.4.1 Artificial Viscosity for the Linear Advection Equation

When the solution is smooth, the CR is sufficient to maintain the stability. However, if there is a discontinuity in the solution, the CR is not sufficient to suppress the numerical oscillations

**Table 1** Implementation schemes for the calculation of the convection term

Scheme	$\nabla\phi$	$\vec{u}$
Scheme 1	VR	VR
Scheme 2	CR	VR
Scheme 3	CR	CR

near the discontinuity. For the linear advection equation, the discontinuity can be introduced through the initial condition. In this case, an AV term in the form of

$$\frac{1}{\Omega_i} \oint_{\partial\Omega_i} \alpha \nabla \phi \cdot \vec{n} dS = \frac{1}{\Omega_i} \sum_{f=1}^{N_f} \int \alpha_f \nabla \phi_f \cdot \vec{n}_f dS \quad (18)$$

is introduced so that the governing equation becomes

$$\bar{\phi}_t + \frac{1}{\Omega_i} \iint_{\Omega_i} \vec{u} \cdot \nabla \phi d\Omega = \frac{1}{\Omega_i} \sum_{f=1}^{N_f} \int \alpha_f \nabla \phi_f \cdot \vec{n}_f dS, \quad (19)$$

where.

$$\alpha_f = \gamma \beta_f |\vec{u}_f \cdot \vec{n}_f| d_f \quad (20)$$

Here the parameter  $\gamma = 0.5$ , and  $d_f$  is the distance between the barycenter of two cells that share the face. The parameter  $\beta_f$  in Eq. (20) is the non-linear coefficient or the shock detector of the AV, which should be very small or even zero when the solution is smooth, and sufficiently large when there is a discontinuity. In the present paper,  $\beta_f$  is based on the smooth indicator defined by.

$$\eta_f = \left| 1 - \frac{2 |\nabla \phi_i(\vec{x}_f) \cdot \vec{n}| |\nabla \phi_j(\vec{x}_f) \cdot \vec{n}|}{|\nabla \phi_i(\vec{x}_f) \cdot \vec{n}|^2 + |\nabla \phi_j(\vec{x}_f) \cdot \vec{n}|^2 + \epsilon} \right|.$$

In smooth region,  $|\nabla \phi_i \cdot \vec{n}| \approx |\nabla \phi_j \cdot \vec{n}|$  so that  $\eta_f$  is very close to zero. When there is a discontinuity, the ratio between  $|\nabla \phi_i \cdot \vec{n}|$  and  $|\nabla \phi_j \cdot \vec{n}|$  will be very large or small and therefore  $\eta_f \approx 1$ . The  $\beta_f$  is determined by  $\eta_f$  through the following equation

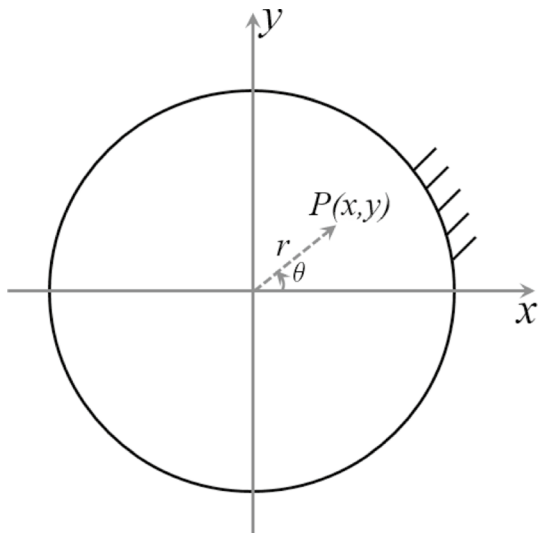
$$\beta_f = \frac{\text{sign}(\eta_f - \eta_{f,c}) + 1}{2} \eta_f \quad (21)$$

where  $\eta_{f,c} = 0.8$  is the threshold of  $\eta_f$ . When  $\eta_f < \eta_{f,c}$ , the solution is considered to be smooth and no AV is introduced. Otherwise the AV is activated by setting  $\beta_f = \eta_f$ .

## 2.4.2 Artificial Viscosity for the Eikonal Equation

In computing the nearest distance to the walls by solving the eikonal equation, there are singularities at local extreme point where the gradient of  $\phi$  is discontinuous. For example, for a circular region shown in Fig. 4, the gradient at point P is  $\nabla \phi = (\frac{-x}{r}, \frac{-y}{r})^T = (-\cos\theta, -\sin\theta)^T$ . Therefore, when  $r \rightarrow 0$ , the gradient at the origin is dependent to the direction and cannot be determined uniquely, which means the gradient is discontinuous at the origin of the circle. In this paper, it is found that when the high order compact FV scheme is used to solve the integral form NCE, there are difficulties in convergence even when the CR scheme is adopted. During the solution procedure, if a spurious local extreme point is formed due to for instance the imperfection in the initial value, it cannot be removed effectively, which may lead to numerical instability sometimes. It is rather straightforward to explain this phenomenon. At the local

**Fig. 4** Schematic figure of the singularity problem



extreme points of  $\phi$ , we have  $\vec{u} = \nabla\phi \sim 0$ . Therefore, there is uncertainty in the upwinding directions. In this case, the CR may not be able to introduce correct upwinding effect.

To solve this problem, an AV term, which is of the same form as that in Eq. (18), is introduced, and the governing equation becomes

$$\bar{\phi}_t + \frac{1}{\Omega_i} \iint_{\Omega_i} \vec{u} \cdot \nabla \phi d\Omega = \frac{1}{\Omega_i} \iint_{\Omega_i} f^2 d\Omega + \frac{1}{\Omega_i} \sum_{f=1}^{N_f} \int \alpha_f \nabla \phi_f \cdot \vec{n}_f dS, \quad (22)$$

However, the specific expressions in the AV term for the eikonal equation are different with those for the linear advection equation. As mentioned earlier, since the gradient singularity problems only appear at the local extreme points, AV should only be activated in the vicinity of the local extreme points to reduce its influence on the accuracy of solutions. In the present paper, we suggest that the AV coefficient takes the same form as the linear advection equation, i.e.

$$\alpha_f = \gamma \beta_f |\nabla \phi_f \cdot \vec{n}_f| d_f \quad (23)$$

but the expression for  $\beta_f$  is different to account for the weak discontinuity in the derivatives

$$\begin{aligned}\beta_f &= \frac{\operatorname{sign}(\eta_f - \eta_{f,c}) + 1}{2} \eta_f \\ \eta_f &= \min\left(\frac{2}{5k^2}, \left|f^2 - |\nabla \phi_f|^2\right|\right) \\ \nabla \phi_f &= \frac{1}{2}(\nabla \phi_i(\vec{x}_f) + \nabla \phi_j(\vec{x}_f)) \\ \eta_{f,c} &= \frac{1}{5k^2} \quad \gamma = 0.5.\end{aligned}$$

In the equations above,  $k$  denotes the reconstruction order, i.e.,  $k=3$  for third-order accurate (quadratic) reconstruction and  $k=4$  for fourth-order accurate (cubic) reconstruction. The  $1/k^2$  term indicates that higher order schemes require smaller AV to stabilize the computation according to the numerical tests. According to Eq. (23), at the very beginning of the computation where  $|f^2 - |\nabla \phi|^2|$  is usually large, an AV coefficient  $\eta_f$  at the order of  $2/5k^2$  is introduced. It is tested in Sect. 4 that  $\eta_f = 2/5k^2$  is large enough to remove the singularity in the solution, and to result in a very fast convergence to steady state. When the numerical solution is nearly converged, the  $|f^2 - |\nabla \phi|^2|$  will be in the order of  $O(\max(\Delta x^k, \Delta y^k))$  in the non-singular regions. When  $\eta_f$  is smaller than  $1/5k^2$ , the AV is turned off so that the accuracy of the solution in these regions is not affected. Only at the local extreme points where  $|f^2 - |\nabla \phi|^2| \rightarrow f^2$ , large AV at the order  $\eta_f = 2/5k^2$  will be introduced to stabilize the computation. Since the AV is diffusive and non-directional, the calculation of the integral form of AV only uses the results of VR.

## 2.5 Time Integration

In this paper, the explicit multistep Runge–Kutta (RK) method is used for time integration. Specifically, the third-order SSP RK method [51]

$$\begin{aligned}\bar{\phi}_i^{(1)} &= \bar{\phi}_i^n + \Delta \tau_i R(\bar{\phi}_i^n), \\ \bar{\phi}_i^{(2)} &= \frac{3}{4} \bar{\phi}_i^n + \frac{1}{4} [\bar{\phi}_i^{(1)} + \Delta \tau_i R(\bar{\phi}_i^{(1)})], \\ \bar{\phi}_i^{n+1} &= \frac{1}{3} \bar{\phi}_i^n + \frac{2}{3} [\bar{\phi}_i^{(2)} + \Delta \tau_i R(\bar{\phi}_i^{(2)})],\end{aligned}\tag{24}$$

is used in the third order accurate scheme, and the four-step fourth-order RK method

$$\begin{aligned}\bar{\phi}_i^{(1)} &= \bar{\phi}_i^n + \frac{\Delta \tau_i}{2} R(\bar{\phi}_i^n), \\ \bar{\phi}_i^{(2)} &= \bar{\phi}_i^n + \frac{\Delta \tau_i}{2} R(\bar{\phi}_i^{(1)}), \\ \bar{\phi}_i^{(3)} &= \bar{\phi}_i^n + \Delta \tau_i R(\bar{\phi}_i^{(2)}), \\ \bar{\phi}_i^{n+1} &= \bar{\phi}_i^n + \frac{\Delta \tau_i}{6} [R(\bar{\phi}_i^n) + 2R(\bar{\phi}_i^{(1)}) + 2R(\bar{\phi}_i^{(2)}) + R(\bar{\phi}_i^{(3)})],\end{aligned}\tag{25}$$

is used in the fourth-order scheme. The time step  $\Delta \tau_i$  of the control volume  $\Omega_i$  is calculated as follows

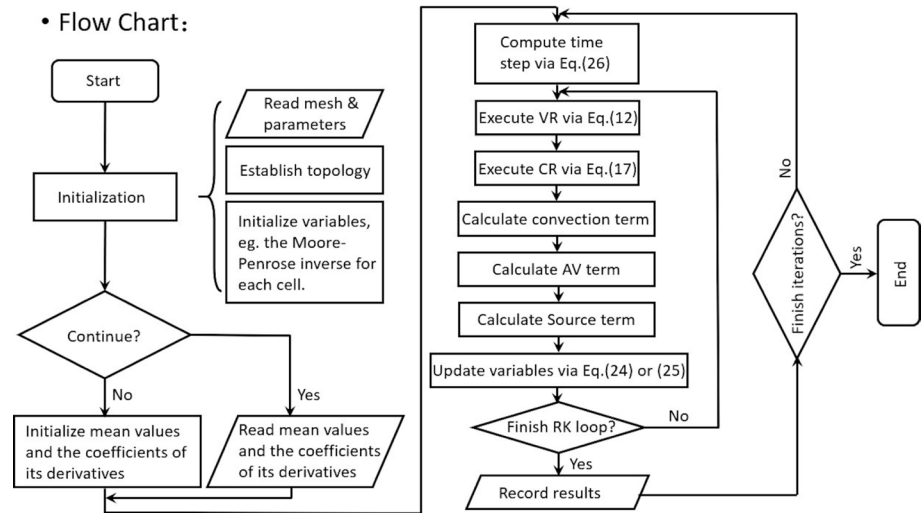


**Fig. 5** Flow chart of the algorithm

$$\Delta\tau_i = \text{CFL} \frac{\overline{\Omega}_i}{\sum_{p=1}^{n_f} (|\vec{u}_{f_p} \cdot \vec{n}_{f_p}| + 1) S_{f_p}}, \quad (26)$$

where  $n_f$  denotes the number of edges of the control volume and  $S_{f_p}$  is length of the  $p$ -th interface of the control volume  $\Omega_i$ , and the residual is the discretized form of

$$R(\phi) = \frac{1}{\Omega_i} \iint_{\Omega_i} (s - \vec{u} \cdot \nabla \phi) d\Omega + \frac{1}{\Omega_i} \sum_{f=1}^{N_f} \int \alpha_f \nabla \phi_f \cdot \vec{n}_f dS.$$

The algorithm of this paper is summarized in Fig. 5.

### 3 Discussions on NCE and CR

In this section, we will take the 1-D Burgers equation as an example to discuss the effect of CR on the FV scheme solving the non-conservative convection equation. The defects of the FV scheme solving the QCE in integral form are also discussed. Before the analysis of the 1-D Burgers equation, we firstly consider a general 1-D non-linear scalar convection equation

$$\frac{\partial \phi}{\partial \tau} + u \frac{\partial \phi}{\partial x} = 0, \quad (27)$$

where  $u = u(\phi)$ . If there exists a function  $f$  satisfying

$$u = \frac{\partial f}{\partial \phi}, \quad (28)$$

Equation (27) can be written in conservation form, i.e.

$$\frac{\partial \phi}{\partial \tau} + \frac{\partial f}{\partial x} = 0.$$

This is the case of Burgers equation, in which  $u = \phi$  and  $f = \frac{1}{2}\phi^2$ . However, if  $f$  in Eq. (28) does not exist, one can only write Eq. (27) into the quasi-conservative form, i.e.

$$\frac{\partial \phi}{\partial \tau} + \frac{\partial u\phi}{\partial x} - \phi \frac{\partial u}{\partial x} = 0. \quad (29)$$

One apparent example of this case is the time dependent eikonal equation discussed in the present paper.

After this general introduction, we now consider the 1-D Burgers equation. As having been discussed, Burgers equation can be written in fully conservative form. There is no problem to solve it using the traditional finite volume schemes. However, here we are interested in the case where it is not written in fully conservative form, but in quasi-conservative form as shown in Eq. (29), since it is just how the eikonal equation is handled in the previous subsections. For the Burgers equation, the quasi-conservative form is

$$\frac{\partial u}{\partial t} + \frac{\partial u^2}{\partial x} - u \frac{\partial u}{\partial x} = 0. \quad (30)$$

Let  $g = \frac{u^2}{2}$ , then Eq. (30) can be expressed as

$$\frac{\partial u}{\partial \tau} + 2 \frac{\partial g}{\partial x} - u \frac{\partial u}{\partial x} = 0. \quad (31)$$

The following discussions will be based on Eq. (31) to present the property of CR and the defects of the FV scheme solving the QCE in integral form.

### 3.1 Property of CR

To simplify the discussion, we consider here the CR based on the linear or degree one polynomial reconstructions. It is apparent that the effect of CR is in close relation to the polynomial reconstruction in terms of the cell averages. To show this effect more clearly, we consider here both upwind and central linear reconstructions instead of the VR. In fact, the linear VR is very close to the central linear reconstruction. To be specific, we only consider the case  $\partial g/\partial u = u > 0$ .

In 1-D case, the linear reconstruction on cell  $\Omega_i$  can be written as

$$u_i(x) = \bar{u}_i + D_i(x - x_i) \quad (32)$$

For the upwind reconstruction assuming  $\partial g/\partial u = u > 0$ ,

$$D_i = \frac{\bar{u}_i - \bar{u}_{i-1}}{\Delta x},$$

and for the central reconstruction,

$$D_i = \frac{\bar{u}_{i+1} - \bar{u}_{i-1}}{2\Delta x}.$$

The linear CR corresponding to Eq. (17) can be derived as follows. At the cell interface located at  $i + 1/2$ , the interfacial value of  $u$  is

$$\hat{u}_{i+1/2} = \frac{1}{2}[1 + \text{sign}(u_{i+1/2})]u_i(x_{i+1/2}) + \frac{1}{2}[1 - \text{sign}(u_{i+1/2})]u_{i+1}(x_{i+1/2}).$$

The assumption  $\partial g/\partial u = u > 0$  leads to

$$\hat{u}_{i+1/2} = u_i(x_{i+1/2}) = \bar{u}_i + \frac{1}{2}D_i\Delta x.$$

Likewise, we have

$$\hat{u}_{i-1/2} = u_{i-1}(x_{i-1/2}) = \bar{u}_{i-1} + \frac{1}{2}D_{i-1}\Delta x.$$

The linear CR is in the following form,

$$\tilde{u}_i(x) = \bar{u}_i + \tilde{D}_i(x - x_i).$$

By minimizing

$$\tilde{I} = \left(\bar{u}_i + \frac{1}{2}\tilde{D}_i\Delta x - \hat{u}_{i+1/2}\right)^2 + \left(\bar{u}_i - \frac{1}{2}\tilde{D}_i\Delta x - \hat{u}_{i-1/2}\right)^2$$

according to Eq. (17), we obtain.

$$\tilde{D}_i = \frac{\hat{u}_{i+1/2} - \hat{u}_{i-1/2}}{\Delta x} = \frac{\bar{u}_i - \bar{u}_{i-1}}{\Delta x} + \frac{1}{2}(D_i - D_{i-1}) \quad (33)$$

Therefore, for the upwind reconstruction,

$$\tilde{D}_i = \frac{3\bar{u}_i - 4\bar{u}_{i-1} + \bar{u}_{i-2}}{2\Delta x}, \quad (34)$$

and for the central reconstruction

$$\tilde{D}_i = \frac{1}{2} \frac{3\bar{u}_i - 4\bar{u}_{i-1} + \bar{u}_{i-2}}{2\Delta x} + \frac{1}{2} \frac{\bar{u}_{i+1} - \bar{u}_{i-1}}{2\Delta x}. \quad (35)$$

Equations (34) and (35) reveal several properties of CR. The first one is that the specific expression of CR is related to the reconstructions that determines the interfacial values, namely the central reconstruction and the upwind reconstruction. The second one is that CR can realize the upwinding effect for both the upwind reconstruction and central reconstruction. Specifically, for the upwind reconstruction,  $\tilde{D}_i$  is the second order upwind approximation to the gradient, and for the central reconstruction,  $\tilde{D}_i$  is the average of the central and upwind approximation of the gradient. And the third one is that CR can maintain the reconstruction accuracy if the reconstruction order of CR is no less than that of the reconstruction to determine the interfacial values.

### 3.2 QCE vs. NCE

In what follows, we consider the FV schemes solving the Burgers equation in different forms. We first consider the integral form of QCE. In this case, the semi-discretized FV scheme is

$$\frac{\partial \bar{u}_i}{\partial \tau} + \frac{2}{\Delta x} (\hat{g}_{i+1/2} - \hat{g}_{i-1/2}) - \frac{1}{\Delta x} \int_{x_{i-1/2}}^{x_{i+1/2}} u_i(x) \frac{\partial u_i(x)}{\partial x} dx = 0.$$

According to Eq. (32), we discuss two cases, which correspond to the upwind reconstruction and central reconstruction.

*Case 1* Upwind reconstruction.

Since  $\partial g / \partial u = u > 0$ , the numerical fluxes  $\hat{g}_{i+1/2}$  and  $\hat{g}_{i-1/2}$  are computed by

$$\begin{cases} \hat{g}_{i+1/2} = \frac{1}{2}(u_{i+1/2}^L)^2 = \frac{1}{2}(\frac{3}{2}\bar{u}_i - \frac{1}{2}\bar{u}_{i-1})^2, \\ \hat{g}_{i-1/2} = \frac{1}{2}(u_{i-1/2}^L)^2 = \frac{1}{2}(\frac{3}{2}\bar{u}_{i-1} - \frac{1}{2}\bar{u}_{i-2})^2. \end{cases}$$

The source term is

$$\frac{1}{\Delta x} \int_{x_{i-1/2}}^{x_{i+1/2}} u_i(x) \frac{\partial u_i(x)}{\partial x} dx = \bar{u}_i \frac{\bar{u}_i - \bar{u}_{i-1}}{\Delta x}.$$

Therefore, the semi-discretized expression of the upwind reconstruction is

$$\frac{\partial \bar{u}_i}{\partial \tau} = -\bar{u}_i \frac{2\bar{u}_i - 3\bar{u}_{i-1} + \bar{u}_{i-2}}{\Delta x} + \frac{(3\bar{u}_i - 4\bar{u}_{i-1} + \bar{u}_{i-2})(\bar{u}_i - 2\bar{u}_{i-1} + \bar{u}_{i-2})}{4\Delta x}. \quad (36)$$

*Case 2* Central reconstruction.

Since  $\partial g / \partial u = u > 0$ , the numerical fluxes  $\hat{g}_{i+1/2}$  and  $\hat{g}_{i-1/2}$  are computed by

$$\begin{cases} \hat{g}_{i+1/2} = \frac{1}{2}(u_{i+1/2}^L)^2 = \frac{1}{2}(\frac{4\bar{u}_i + \bar{u}_{i+1} - \bar{u}_{i-1}}{4})^2, \\ \hat{g}_{i-1/2} = \frac{1}{2}(u_{i-1/2}^L)^2 = \frac{1}{2}(\frac{4\bar{u}_{i-1} + \bar{u}_i - \bar{u}_{i-2}}{4})^2. \end{cases}$$

The volume integration can be obtained by

$$\frac{1}{\Delta x} \int_{x_{i-1/2}}^{x_{i+1/2}} u_i(x) \frac{\partial u_i(x)}{\partial x} dx = \bar{u}_i \frac{\bar{u}_{i+1} - \bar{u}_{i-1}}{2\Delta x}.$$

Therefore, the semi-discretized expression of central reconstruction is

$$\frac{\partial \bar{u}_i}{\partial \tau} = -\bar{u}_i \frac{3\bar{u}_i - 4\bar{u}_{i-1} + \bar{u}_{i-2}}{2\Delta x} - \frac{(\bar{u}_{i+1} - 3\bar{u}_i + 3\bar{u}_{i-1} - \bar{u}_{i-2})(\bar{u}_{i+1} + 3\bar{u}_i - 5\bar{u}_{i-1} + \bar{u}_{i-2})}{16\Delta x}. \quad (37)$$

Next, we consider the integral form of NCE. In this case, the semi-discretized FV scheme is

$$\frac{\partial \bar{u}_i}{\partial \tau} + \frac{1}{\Delta x} \int_{x_{i-1/2}}^{x_{i+1/2}} \tilde{u}_i(x) \frac{\partial \tilde{u}_i(x)}{\partial x} dx = 0.$$

According to Eqs. (34) and (35), we also discuss two cases, which correspond to the CR constructed by upwind reconstruction and central reconstruction.

*Case 3* CR corresponding to upwind construction.

According to Eq. (34), the volume integration can be expressed by

$$\frac{1}{\Delta x} \int_{x_{i-1/2}}^{x_{i+1/2}} \tilde{u}_i(x) \frac{\partial \tilde{u}_i(x)}{\partial x} dx = \bar{u}_i \frac{3\bar{u}_i - 4\bar{u}_{i-1} + \bar{u}_{i-2}}{2\Delta x}.$$

Therefore, the semi-discretized expression is

$$\frac{\partial \bar{u}_i}{\partial \tau} = -\bar{u}_i \frac{3\bar{u}_i - 4\bar{u}_{i-1} + \bar{u}_{i-2}}{2\Delta x}. \quad (38)$$

*Case 4* CR corresponding to central construction.

According to Eq. (35), the volume integration can be expressed by

$$\frac{1}{\Delta x} \int_{x_{i-1/2}}^{x_{i+1/2}} \tilde{u}_i(x) \frac{\partial \tilde{u}_i(x)}{\partial x} dx = \bar{u}_i \left( \frac{1}{2} \frac{3\bar{u}_i - 4\bar{u}_{i-1} + \bar{u}_{i-2}}{2\Delta x} + \frac{1}{2} \frac{\bar{u}_{i+1} - \bar{u}_{i-1}}{2\Delta x} \right).$$

Therefore, the semi-discretized expression is

$$\frac{\partial \bar{u}_i}{\partial \tau} = -\bar{u}_i \left( \frac{1}{2} \frac{3\bar{u}_i - 4\bar{u}_{i-1} + \bar{u}_{i-2}}{2\Delta x} + \frac{1}{2} \frac{\bar{u}_{i+1} - \bar{u}_{i-1}}{2\Delta x} \right). \quad (39)$$

To analyze the dissipation property of the semi-discretized expressions (36)–(39), we adopt the methods provided in References [52], [53]. The Taylor expansion of a smooth function  $u(x)$  at  $x_i$  can be expressed as

$$\begin{aligned} u(x) &= u(x_i) + u'(x_i)(x - x_i) + \frac{1}{2!} u''(x_i)(x - x_i)^2 + \frac{1}{3!} u^{(3)}(x_i)(x - x_i)^3 \\ &\quad + \frac{1}{4!} u^{(4)}(x_i)(x - x_i)^4 + \frac{1}{5!} u^{(5)}(x_i)(x - x_i)^5 + O((x - x_i)^6). \end{aligned} \quad (40)$$

Integrating Expression (40) on control volume  $\Omega_i = [x_{i-1/2}, x_{i+1/2}]$ , we have the following expression

$$\bar{u}_i = u(x_i) + \frac{\Delta x^2}{24} u''(x_i) + \frac{\Delta x^4}{1920} u^{(4)}(x_i) + O(\Delta x^6), \quad (41)$$

In a similar way, we obtain the expansion expressions of  $\bar{u}_{i-2}$ ,  $\bar{u}_{i-1}$  and  $\bar{u}_{i+1}$ , as

$$\begin{aligned} \bar{u}_{i-2} &= u(x_i) - 2\Delta x u'(x_i) + \frac{49}{24} \Delta x^2 u''(x_i) - \frac{17}{12} \Delta x^3 u^{(3)}(x_i) + \frac{1441}{1920} \Delta x^4 u^{(4)}(x_i) + O(\Delta x^5), \\ \bar{u}_{i-1} &= u(x_i) - \Delta x u'(x_i) + \frac{13}{24} \Delta x^2 u''(x_i) - \frac{5}{24} \Delta x^3 u^{(3)}(x_i) + \frac{121}{1920} \Delta x^4 u^{(4)}(x_i) + O(\Delta x^5), \\ \bar{u}_{i+1} &= u(x_i) + \Delta x u'(x_i) + \frac{13}{24} \Delta x^2 u''(x_i) + \frac{5}{24} \Delta x^3 u^{(3)}(x_i) + \frac{121}{1920} \Delta x^4 u^{(4)}(x_i) + O(\Delta x^5), \end{aligned} \quad (42)$$

Substituting Equations (41) and (42) into the semi-discretized expressions (36)–(39), we have the following expression

$$\frac{\partial \bar{u}_i}{\partial \tau} = -\bar{u}_i u'(x_i) + C_i + D_i + HOT, \quad (43)$$

where  $C_i$  corresponds to the dominant dispersion terms,  $D_i$  corresponds to the dominant dissipation terms, and  $HOT$  corresponds to the higher order terms. The specific expressions for Case 1–4 are summarized as

#### Case 1

$$\begin{aligned} C_i &= \frac{19}{24} \Delta x^2 \bar{u}_i u^{(3)}(x_i), \\ D_i &= -\left[ \frac{1}{2} \Delta x \bar{u}_i + \frac{1}{2} \Delta x^2 u'(x_i) \right] u''(x_i) - \left[ \frac{9}{16} \Delta x^3 \bar{u}_i + \frac{5}{16} \Delta x^4 u'(x_i) \right] u^{(4)}(x_i), \\ HOT &= \frac{7}{48} \Delta x^4 u^{(3)}(x_i) u''(x_i) + O(\Delta x^5). \end{aligned} \quad (44)$$

#### Case 2

$$\begin{aligned} C_i &= \frac{7}{24} \Delta x^2 \bar{u}_i u^{(3)}(x_i), \\ D_i &= -\left[ \frac{1}{4} \Delta x^3 \bar{u}_i - \frac{1}{8} \Delta x^4 u'(x_i) \right] u^{(4)}(x_i), \\ HOT &= -\frac{1}{4} \Delta x^3 u^{(3)}(x_i) u'(x_i) + O(\Delta x^5). \end{aligned} \quad (45)$$

#### Case 3

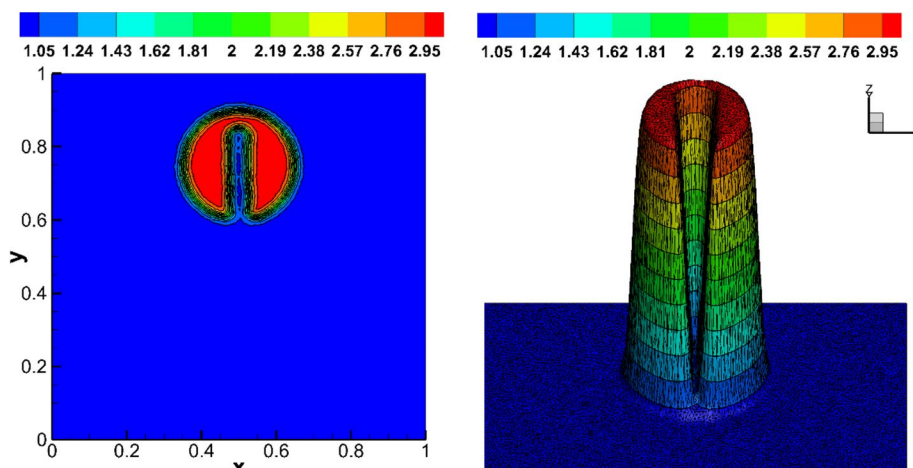
$$\begin{aligned} C_i &= \frac{7}{24} \Delta x^2 \bar{u}_i u^{(3)}(x_i), \\ D_i &= -\frac{1}{4} \Delta x^3 \bar{u}_i u^{(4)}(x_i), \\ HOT &= \frac{749}{5760} \Delta x^4 \bar{u}_i u^{(5)}(x_i) + O(\Delta x^5). \end{aligned} \quad (46)$$

#### Case 4

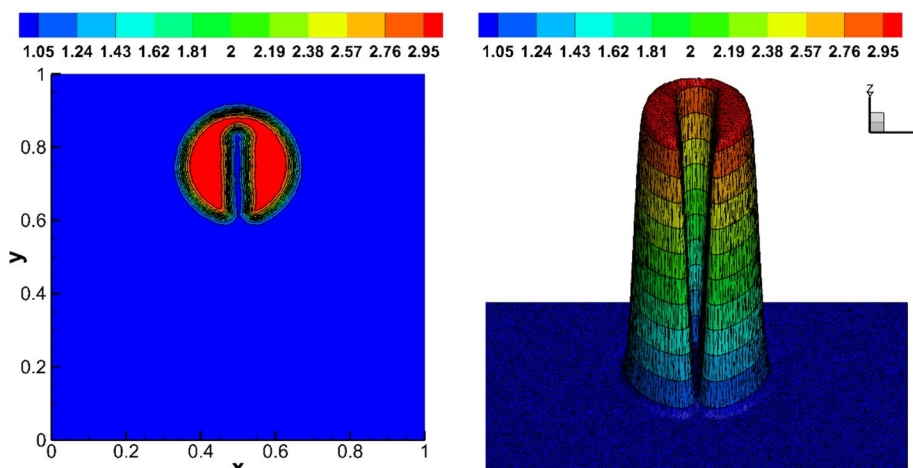
$$\begin{aligned} C_i &= \frac{1}{24} \Delta x^2 \bar{u}_i u^{(3)}(x_i), \\ D_i &= -\frac{1}{8} \Delta x^3 \bar{u}_i u^{(4)}(x_i), \\ HOT &= \frac{329}{5760} \Delta x^4 \bar{u}_i u^{(5)}(x_i) + O(\Delta x^5). \end{aligned} \quad (47)$$

Expressions (44)–(47) are the modified equations of the corresponding semi-discretized FV schemes. According to Expression (44), i.e., the case of solving integral form of QCE based on upwind reconstruction, we find the coefficients of the second-order derivative at the right hand side are mainly determined by  $-\frac{1}{2} \bar{u}_i \Delta x$ , which is negative since  $\bar{u}_i > 0$ . Therefore, the numerical stability still cannot be ensured during the computation. Expression (45), which corresponds to the case that solves integral form of QCE based on central reconstruction, also indicates the same possibility, since it is possible that  $-\frac{1}{8} u'(x_i) \Delta x^4$  is larger than  $\frac{1}{4} \bar{u}_i \Delta x^3$  for the region that  $u(x)$  changes sharply. Therefore, Expressions (44) and (45) show that the numerical instability is possible to occur when solving the integral form of QCE using either the upwind or central reconstruction. On the other hand, expressions (46) and (47) indicate that when the integral form of NCE is solved with CR, the numerical

stability can be guaranteed whether the upwind or the central reconstruction is used to calculated the interfacial values, since  $-\frac{1}{4}\bar{u}_i\Delta x^3$  or  $-\frac{1}{8}\bar{u}_i\Delta x^3$ , which is the coefficient of the fourth-order derivatives, is negative. This comparison confirms the importance of solving NCE using CR. We should notice that if one solves NCE without using CR, the resulting scheme is a purely central scheme, which is usually not stable.



(a) Third-order FVM



(b) Fourth-order FVM

**Fig. 6** The distribution of the numerical solutions after a period of rotation

**Fig. 7** Comparison of the isoline 0.5 between the numerical and reference solutions after half of a period

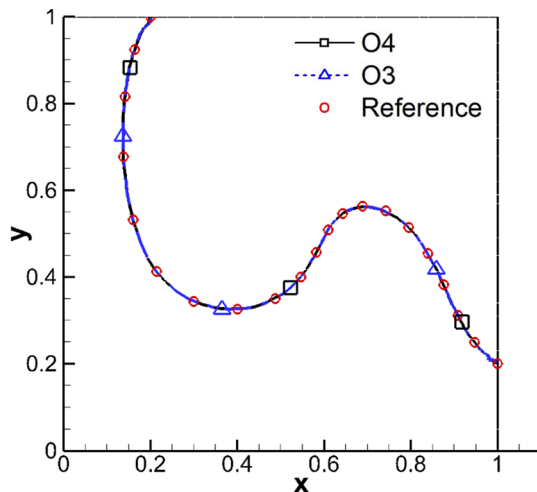


**Fig. 8** Comparison of the isoline 0.5 between the numerical and reference solutions after one period

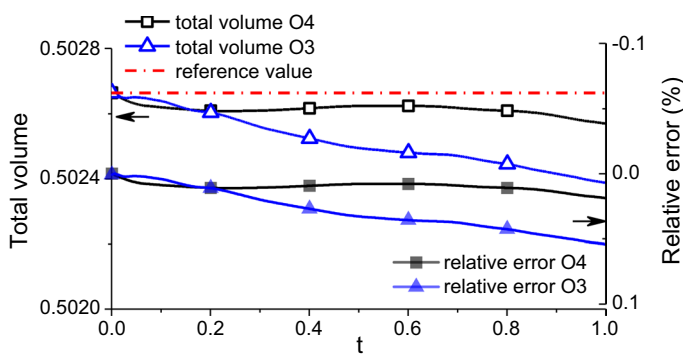
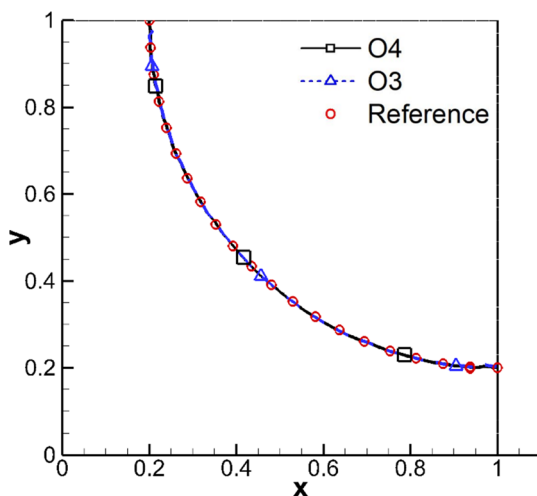


**Fig. 9** The change of total volume  $Vol = \iint_D \phi(x, y) dx dy$  and its relative error

## 4 Results and Discussions

In this section, several test cases are solved using the numerical schemes proposed in the present paper. We will consider the case of solving the linear advection equation, Eq.(19), as well as the eikonal equation, Eq. (22) with  $f = 1$ . Specifically, the latter one corresponds to the calculation of the nearest distance to given solid walls.

### 4.1 The Results of the Linear Advection Equation

#### 4.1.1 The Rotating Slotted Cylinder Problem

In this sub-section, the well-known rotating slotted cylinder problem [54] will be used to test the capability of the proposed method in this paper to handle the discontinuity. The governing equation is Eq. (5), with  $s = 0$  and the specified advection velocity  $\vec{u} = (-\omega(y - y_0), \omega(x - x_0))^T$ . Therefore, the CR will be used for calculating the quantity being transported, i.e.,  $\nabla\phi$ . The initial condition is

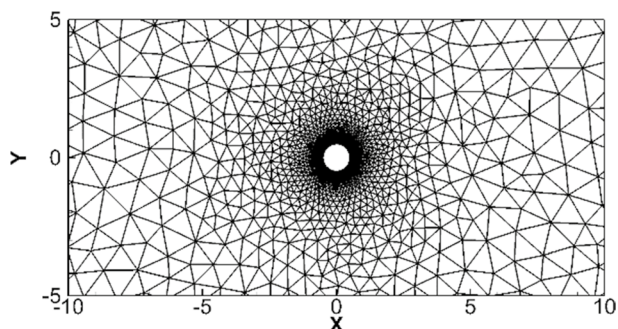
$$\phi_0 = \begin{cases} 3, & \text{inside the slotted cylinder} \\ 1, & \text{outside the slotted cylinder} \end{cases}$$

And the boundary condition is  $\phi_b = 1$ . The test will be conducted on an unstructured triangular mesh, with the computational domain  $D = [0, 1] \times [0, 1][0, 1]$ . The computational

**Table 2** Test cases

Order	nontreated	AV	CR	AV+CR
O=3	Case O3_Non	Case O3_AV	Case O3_CR	Case O3_AV+CR
O=4	Case O4_Non	Case O4_AV	Case O4_CR	Case O4_AV+CR

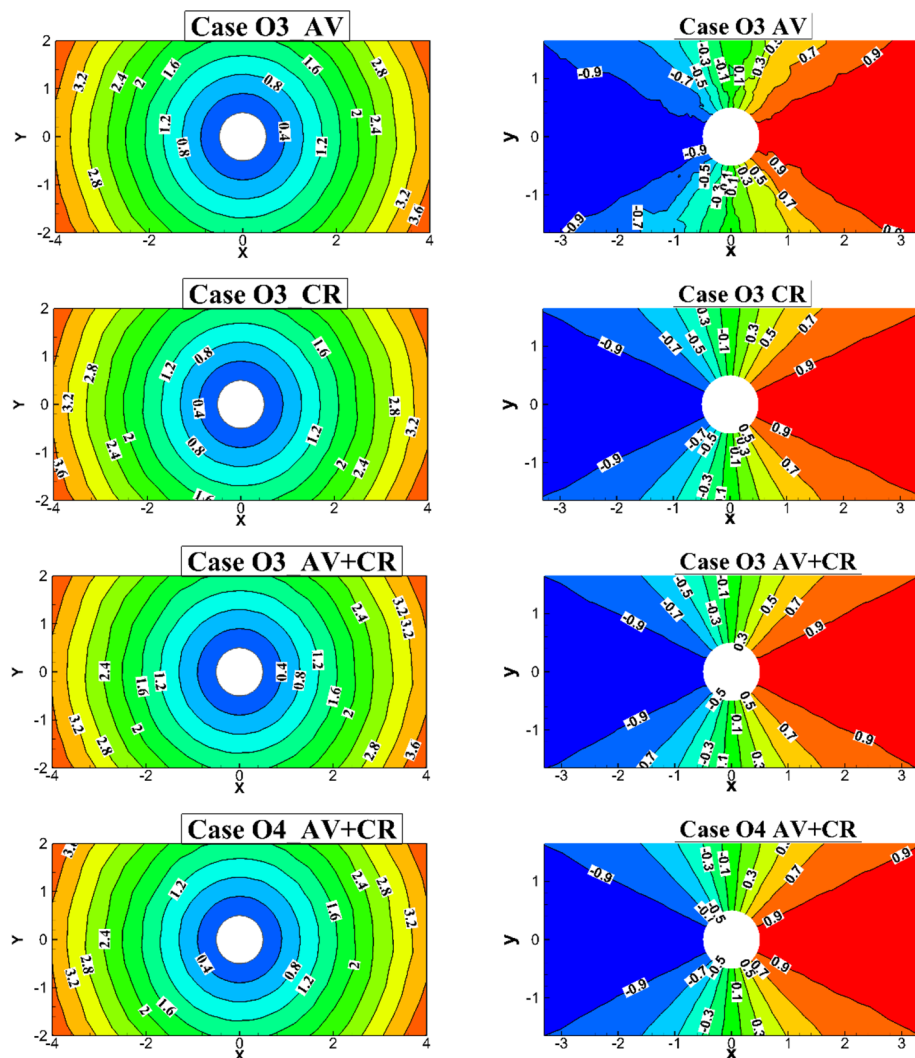
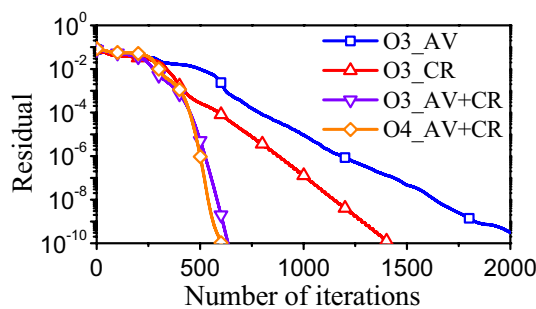
**Fig. 10** Computational grid



**Table 3** Results of third-order and fourth order schemes

	Case O3_Non	Case O3_AV	Case O3_CR	Case O3_AV+CR
Results	Divergent	Convergent (problematic)	Convergent	Convergent
	Case O4_Non	Case O4_AV	Case O4_CR	Case O4_AV+CR
Results	Divergent	Divergent	Divergent	Convergent

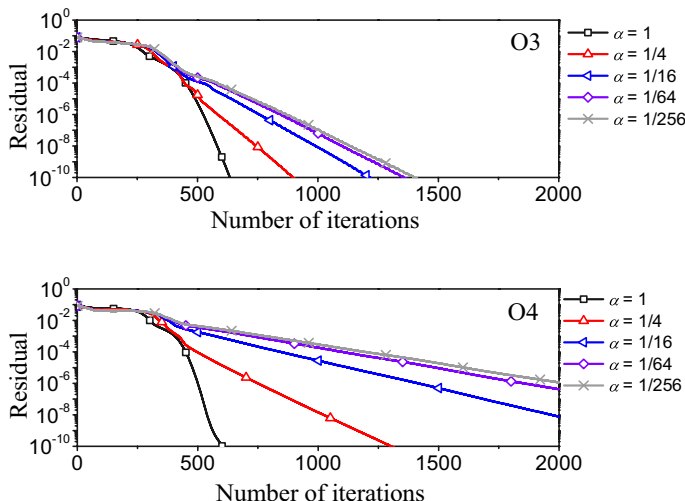
**Fig. 11** Residuals of part of test cases



**Fig. 12** The calculated results: the minimum wall distance (left column), the partial derivative of the minimum wall distance with respect to  $x$  (right column)

**Table 4** Test cases

$\alpha$	1	1/4	1/16	1/64	1/256
----------	---	-----	------	------	-------

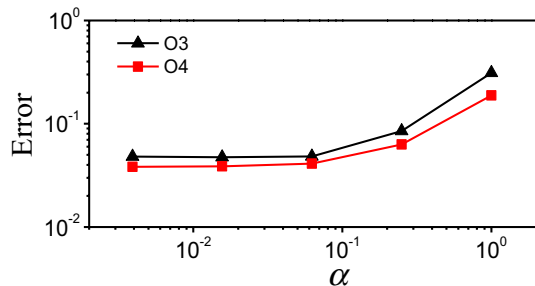
**Fig. 13** Residuals of test cases

domain is discretized by triangle cells, there are 101 nodes on each boundary edge, and the total cell number is 31210. The angular velocity  $\omega = 200\pi$ . The simulation is carried out for one period till  $T = 10^{-2}$ , and global time step  $\Delta t = 10^{-5}$  is used in the computation. It should be noted that this test problem is unsteady, and the reconstruction iteration should be conducted until to a convergent state is achieved in each time step. Both the third- and fourth-order FVM are used to solve the problem, and their results will be compared and discussed.

Figure 6 presents the distribution of the numerical solutions after a period of rotation. Firstly, the shape of the slotted cylinder is preserved well due to the upwinding property of CR. Secondly, owing to the effect of the AV, there is no spurious oscillations near the discontinuities. Therefore, we can conclude that combining the use of CR and AV is an effective way to deal with the evolution of discontinuous solutions of the non-conservative governing equations, even for the high-order methods. In addition, we can find that the results of the fourth-order method are slightly better than those of the third-order counterparts, i.e., the filling-in of the gap and the erosion of the “bridge” of the fourth-order method slightly less severe than those of the third-order one.

#### 4.1.2 The Swirling Deformation Flow Problem

In this sub-section, the swirling deformation flow problem [55] will be used to test the volume preserving performance of the proposed method. The governing equation is Eq. (5), with  $s = 0$  and the specified advection velocity  $\bar{u} = (\sin^2(\pi x) \sin(2\pi y)g(t), -\sin^2(\pi y) \sin(2\pi x)g(t))^T$ . The initial condition is

**Fig. 14** Errors of test cases

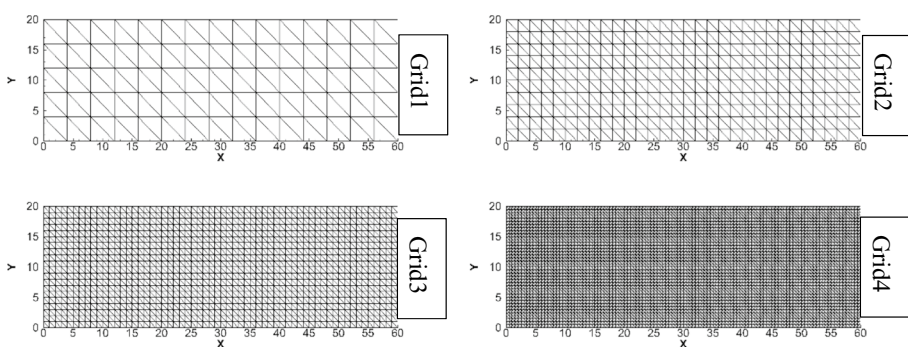
$$\phi_0 = \begin{cases} 1, & d(\vec{x}, \vec{x}_0) < 0.8 \\ 0, & \text{others} \end{cases}$$

with  $\vec{x}_0 = (1, 1)^T$ , and the boundary condition is

$$\phi_b = \begin{cases} 1, & d(\vec{x}_b, \vec{x}_0) < 0.8 \\ 0, & \text{others} \end{cases}$$

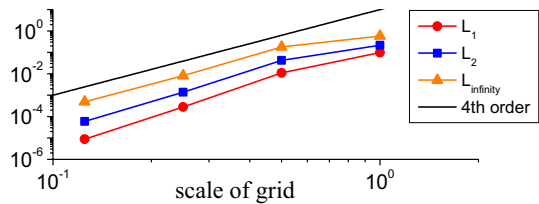
Similar with test in 4.1.1, the CR and AV method will be adopted to calculate the quantity being transported and ensure the stability of computation, respectively. The computational domain and mesh are the same as those in test case 1. It is to be noted that owing to the characteristics of the computational domain and the advection velocity, the integral of the quantity on the whole computational domain  $\text{Vol} = \iint_D \phi(x, y, t) dx dy$  is a constant. This property provides a reference to test the volume preserving performance of the proposed method. We choose  $g(t) = \cos(\pi t/T_0)$ , with  $T_0 = 1$ . The period of the solution is  $T = 2$ , and global time step is used in the computation, with  $\Delta t = 10^{-3}$ . Both the third- and fourth-order FVM are used to solve the problem, and their results will be compared and discussed.

Figures 7 and 8 present the comparison of the isoline 0.5 between the numerical solutions after half a period and one period, respectively. The reference solution is obtained by means of the characteristic theory using the fourth-order RK method to evolve the initial curve to the current stage. The reason for choosing the isoline 0.5 is to eliminate the influence of dissipation on the evaluation of volume preserving performance. It can be found that the numerical isolines are overlapped with the reference solution. On the other hand,

**Fig. 15** Computational grids of the test cases

**Table 5** Wall distance errors and accuracy orders for the test cases

	Scale of grid	$L_1$ error	Order	$L_2$ error	Order	$L_\infty$ error	Order
Grid1	1	9.780E-2		2.161E-1		5.830E-1	
Grid2	1/2	1.097E-2	3.156	4.202E-2	2.363	1.775E-1	1.715
Grid3	1/4	2.774E-4	5.306	1.380E-3	4.928	8.170E-3	4.442
Grid4	1/8	8.693E-6	4.996	5.905E-5	4.547	4.939E-4	4.048

**Fig. 16** Reconstructed orders of the test cases

the total volume  $\text{Vol} = \iint_D \phi(x, y) dx dy$  is also preserved well, and the maximum relative error is less than 0.02% for the fourth-order method. For the third-order method, due to a larger dissipation, the maximum relative error is about 0.06%, which still is a small value. Therefore, the above discussion demonstrates the good volume preserving performance of the present method (Fig. 9).

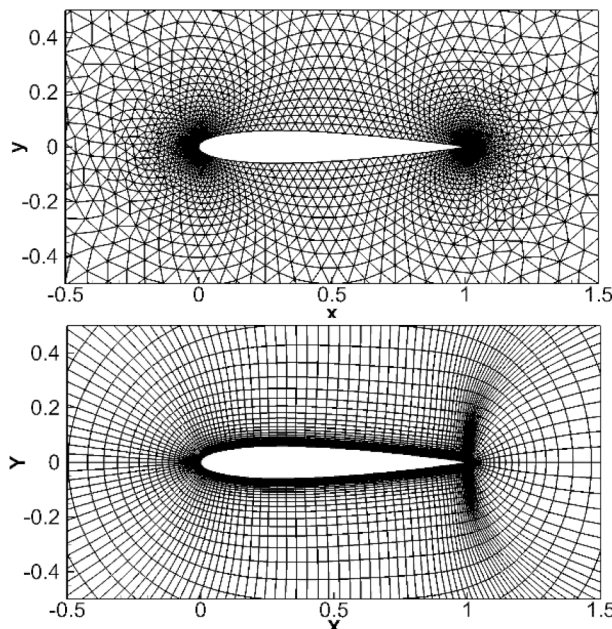
## 4.2 The Results of the Eikonal Equation

### 4.2.1 Necessity of CR and AV

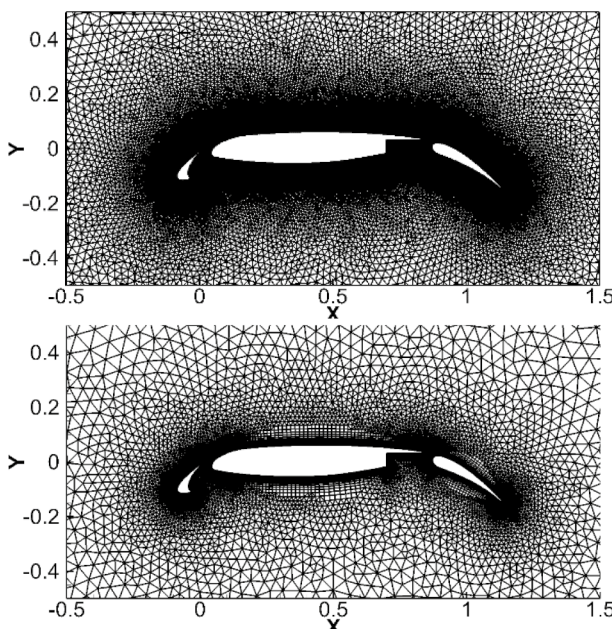
In this sub-section, the minimum wall distance to a circular cylinder problem is solved to test the effects of CR and AV. This test case is numerically solved using both the third-order and fourth-order schemes. The specific numerical recipes are summarized in Table 2. The nontreated case means that the integral convection term  $\iint_{\Omega_i} \vec{u} \cdot \nabla \phi d\Omega$  is computed directly in terms of VR. Other cases correspond to the uses of only AV, only CR and both AV and CR. The AV coefficient is set to be constant, i.e.,  $\beta_f = \frac{2}{5k^2}$ . The computational grid is composed of 5566 triangular elements as shown in Fig. 10. The time integration adopts the third-order SSP RK method, i.e., Eq. (24), with CFL=0.6. The computation is started from the initial value  $\phi_0(\vec{x}) = 0$ .

Table 3 presents the results of each test cases. Figure 11 shows the residuals for the convergent cases. And Fig. 12 shows the calculated minimum wall distances and their partial derivatives with respect to  $x$  for the convergent cases. When the integral convection term  $\iint_{\Omega_i} \vec{u} \cdot \nabla \phi d\Omega$  is computed directly in terms of VR, both the computations using the third-order and fourth-order schemes are divergent, which indicates the occurrences of the numerical instability.

When only the AV is used, the third-order scheme is convergent. However, it can be clearly seen from Fig. 8 that  $\partial\phi/\partial x$  is predicted with spurious oscillations. The fourth-order scheme is divergent. These results show that the use of AV is helpful in obtaining

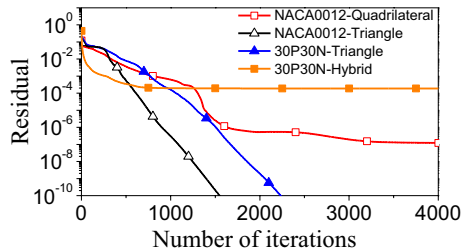


(a) NACA0012



(b) 30P30N

**Fig. 17** Computational grids

**Fig. 18** Residuals of test cases

the convergent solution for the third order scheme, and is not sufficient for the fourth order scheme.

When only the CR is used, the third-order scheme is convergent, and both the minimum wall distances and their partial derivatives are correctly calculated. Again the fourth-order scheme is divergent. This confirms the discussion in Sect. 2.4, that the CR cannot introduce correct upwinding effect since  $\vec{u} = \nabla\phi \sim 0$  means the uncertainty in the upwinding directions.

When both the AV and CR are used, both the third-order and fourth-order schemes are convergent, and residuals of the two cases decrease rapidly as shown in Fig. 7. Consequently, we have shown that the numerical instability arises from solving the eikonal equation in the QCE form can be effectively resolved by solving the NCE with additional CR and AV techniques.

#### 4.2.2 The Effect of AV Coefficient

According to the previous discussions, AV is helpful to improve the stability of the calculations. However, AV also changes the equation. Therefore, it is necessary to evaluate the influence of AV coefficient on the accuracy of the solutions. In this section, both the third- and fourth-order VR and CR are used, and the computational grid and the computational settings are the same as those in Sect. 4.1 except that we use  $\beta_f = \frac{2\alpha}{5k^2}$ . We will use a series of  $\alpha$  to alter the coefficient of AV, and the detailed information for the test cases are listed in Table 4.

Figure 13 shows the residuals of each test cases, and Fig. 14 shows the corresponding errors. According to Fig. 13, the larger the AV coefficient, the faster the convergence speed, and vice versa. However, when the AV coefficient is small enough, it has little effect on the convergence speed. On the other hand, according to Fig. 14, a larger AV coefficient also produces a larger error. And when the AV is small enough, the error does not change with the AV coefficient. In practice, the AV coefficient is given by Eq.(23). The tests in this sub-section indicate that Eq.(23) is in perfect balance between the convergence speed and numerical error.

#### 4.2.3 Accuracy Test

In this sub-section, the proposed scheme with both CR and AV is applied to the minimum wall distance to a straight wall to study its accuracy. As shown in Fig. 15, four sets of computational grids are used with respectively 150, 600, 2400 and 9600 cells. The computational domain is rectangle, the left side and right side of the domain are both periodic boundaries, while the top side and bottom side are far-field and wall boundaries, respectively. The AV coefficient is given by Eq. (23). The time integration adopts the fourth-order

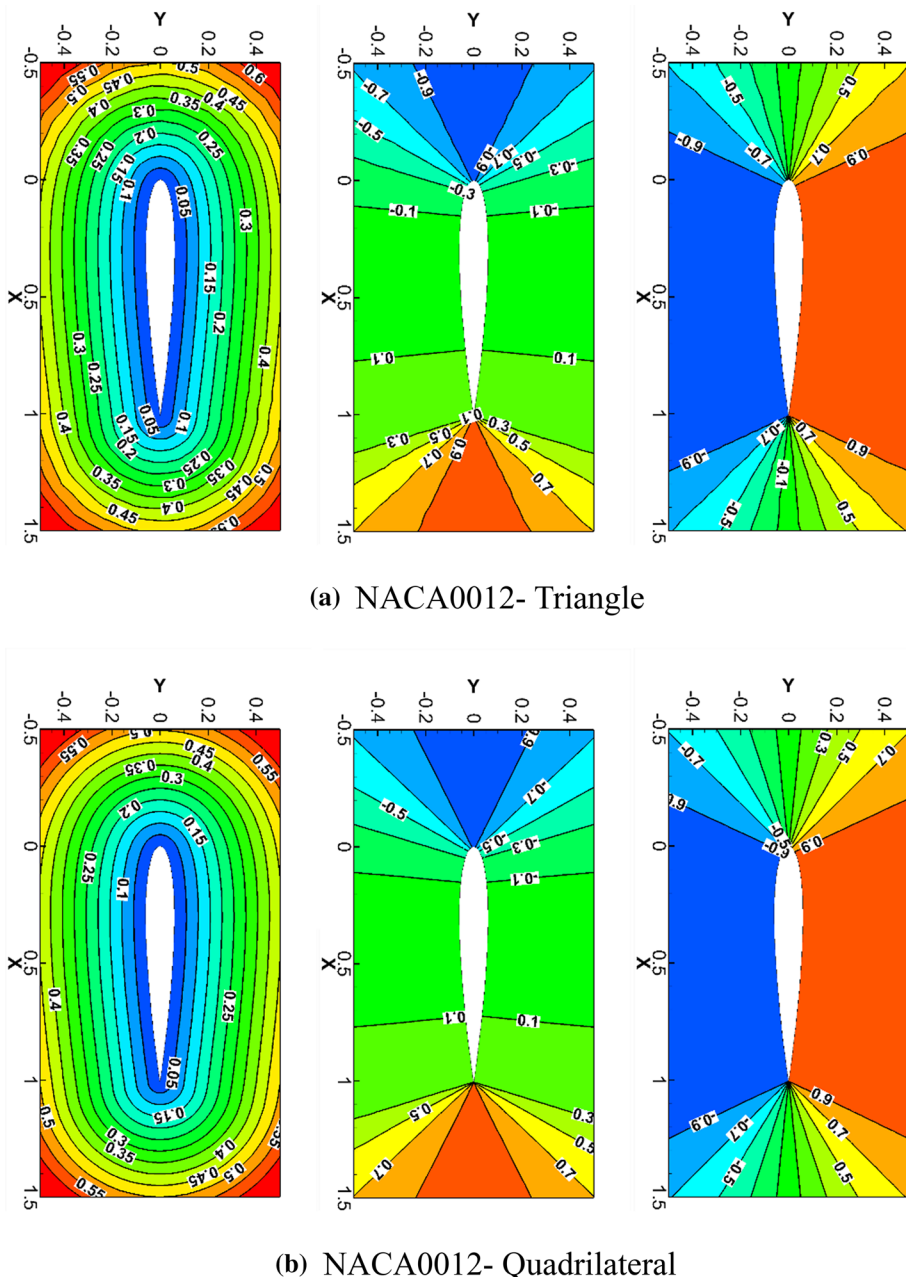


**Fig. 19** Results of NACA0012: Minimum wall distance (left), the partial derivatives of the minimum wall distance with respect to  $x$  (mid) and  $y$  (right)

RK method, i.e., Eq. (25), with  $\text{CFL}=0.5$ . The computation is stated from initial guess of the solution,  $\phi_0(\vec{x}) = 0$ . Table 5 presents the wall distance errors and accuracy orders for the test cases. Figure 16 shows the calculated  $L_1$ ,  $L_2$  and  $L_\infty$  error norms versus the scale of

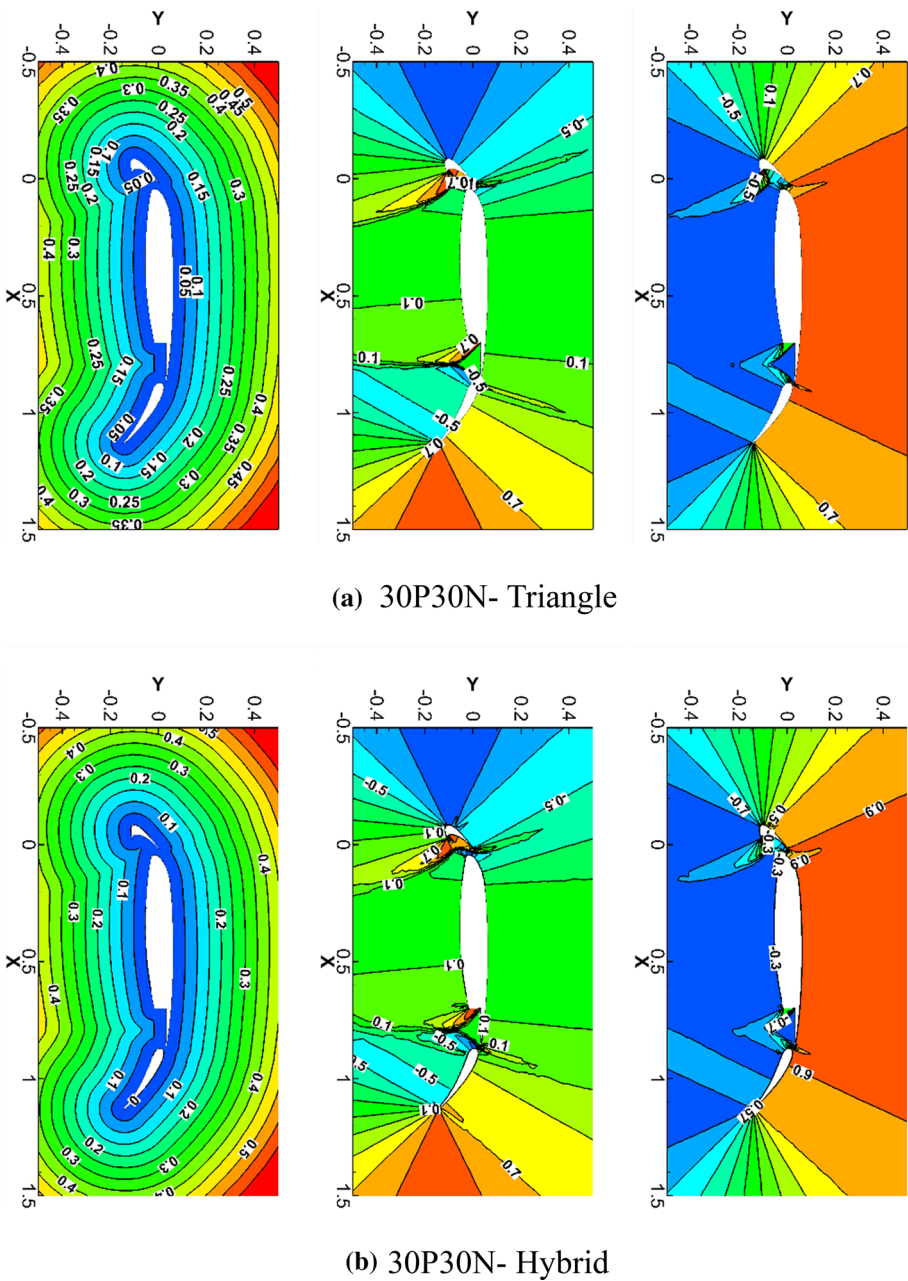


**Fig. 20** Results of 30P30N: Minimum wall distance (left), the partial derivatives of the minimum wall distance with respect to  $x$  (mid) and  $y$  (right)

grids on the four sets of grids. According to Table 5 and Fig. 16, the rates of convergence using the three norms are almost all higher than the VR and CR. Therefore, if we choose

the order of CR is no less than that of VR, the order of accuracy of the scheme will not be affected.

#### 4.2.4 Results of Complex Geometric Configurations

This sub-section tests the capability of the proposed numerical scheme in computing the minimum wall distance to walls with more complicated geometric configurations. The shapes of the walls are chosen to be the NACA0012 airfoil and the 30P30N high lift configuration. For NACA0012, we use a triangular mesh with 9164 cells and a quadrilateral mesh with 12,800 cells. For 30P30N, we use triangular grids with 65,072 cells and a hybrid mesh with 30,125 quadrilateral cells and 23,745 triangular cells. In this section, fourth-order VR and CR are used, and the computational grids are shown in Fig. 17. The AV coefficient is given by Eq. (23). The time integration adopts the third-order SSP RK method, i.e., Eq. (24), with  $CFL = 0.6$ . All of the computations are started from  $\phi_0(\vec{x}) = 0$ .

Figure 18 presents the time histories of residuals for each test cases, the results shows that when there is not local extreme point in the solution such as the NACA 0012 case, the residuals can reach machine zero. When there are local extreme points, the residuals could not reach machine zero since the AV is activated, such as the 30P30N case. Figures 19 and 20 show the calculated minimum wall distances and their partial derivatives with respect to  $x$  and  $y$  for NACA0012 and 30P30N, respectively. According to Fig. 19, we find the calculated results on triangle grid are very close to those on quadrilateral grid, with the quadrilateral grid result being slightly smoother. Figure 20 demonstrates that the method is capable of computing the case with multiple walls and local extrema in the solution.

## 5 Conclusions

The high order numerical procedure on the unstructured grids for solving the linear advection equation in non-conservative form and the eikonal equation in its time-dependent form is studied in the present paper. The compact FV schemes based on the VR have been applied successfully in solving the Euler and Navier–Stokes equations. However, when they are applied to solve the time-dependent eikonal QCE, numerical instabilities are observed. One finding of this paper is that the instabilities are associated with QCE. As a remedy, we propose to solve the NCE using the FV schemes. To account for the unwinding effect, the CR is designed, which is a numerical approximation procedure based on the VR and a state Riemann solver. Another finding of this paper is that CR may not be able to introduce sufficient upwinding effect at local extrema. To stabilize the computation, additional AV should be introduced. The coefficient of the AV is chosen so that it is large in the beginning of the computation and at the local extreme points, and very small in regions with small residuals. The test results show that the proposed compact FV scheme is very accurate and robust. The methods proposed in this paper not only provide effective numerical schemes solving the linear advection equation and the transport eikonal equation, but also provide a new idea for solving other non-conservative equations using high order FV schemes.

**Acknowledgements** This work is supported by the China Postdoctoral Science Foundation under Grant No. 2019M660613, the national numerical wind tunnel project, and Project 91752114 of NSFC.

**Author Contributions** All authors contributed to the study conception and design based on the initial idea of YR. The numerical schemes, coding and data processing were carried out by QH based on the code developed by QW. The first draft of the manuscript was written by QH and all authors commented on previous versions of the manuscript. All authors read and approved the final manuscript.

**Data Availability** Parts of the data and materials are available upon request.

## Declarations

**Conflict of interest** The authors declare that they have no conflict of interest.

## References

1. Wang, Q., Ren, Y.X., Li, W.: Compact high order finite volume method on unstructured grids I: basic formulations and one-dimensional schemes. *J. Comput. Phys.* **314**, 863–882 (2016)
2. Wang, Q., Ren, Y.X., Li, W.: Compact high order finite volume method on unstructured grids II: extension to two-dimensional Euler equations. *J. Comput. Phys.* **314**, 883–908 (2016)
3. Wang, Q., Ren, Y.X., Pan, J., et al.: Compact high order finite volume method on unstructured grids III: variational reconstruction[J]. *J. Comput. Phys.* **337**, 1–26 (2017)
4. Zhang, Y.S., Ren, Y.X., Wang, Q.: Compact high order finite volume method on unstructured grids IV: explicit multi-step reconstruction schemes on compact stencil[J]. *J. Comput. Phys.* **396**, 161–192 (2019)
5. Pan, J., Ren, Y.X., Sun, Y.: High order sub-cell finite volume schemes for solving hyperbolic conservation laws II: extension to two-dimensional systems on unstructured grids[J]. *J. Comput. Phys.* **338**, 165–198 (2017)
6. Bassi, F., Rebay, S.: High-order accurate discontinuous finite element solution of the 2D Euler equations. *J. Comput. Phys.* **138**(2), 251–285 (1997)
7. Bassi, F., Rebay, S.: A high-order accurate discontinuous finite element method for the numerical solution of the compressible Navier–Stokes equations. *J. Comput. Phys.* **131**(2), 267–279 (1997)
8. Cockburn, B., Shu, C.W.: Runge–Kutta discontinuous Galerkin methods for convection-dominated problems. *J. Sci. Comput.* **16**(3), 173–261 (2001)
9. Romero, J., Asthana, K., Jameson, A.: A simplified formulation of the flux reconstruction method[M]. Plenum Press, New York (2016)
10. Huynh HT. A flux reconstruction approach to high-order schemes including discontinuous Galerkin methods. In: 18th AIAA Computational Fluid Dynamics Conference p. 4079 (2007)
11. Wang, Z.J., Gao, H.: A unifying lifting collocation penalty formulation including the discontinuous Galerkin, spectral volume/difference methods for conservation laws on mixed grids[J]. *J. Comput. Phys.* **228**(21), 8161–8186 (2009)
12. Dumbser, M., Balsara, D.S., Toro, E.F., et al.: A unified framework for the construction of one-step finite volume and discontinuous Galerkin schemes on unstructured meshes[J]. *J. Comput. Phys.* **227**(18), 8209–8253 (2008)
13. Zhang, L., Wei, L., He, L.X., et al.: A class of hybrid DG/FV methods for conservation laws I: basic formulation and one-dimensional systems[J]. *J. Comput. Phys.* **231**(4), 1081–1103 (2012)
14. Zhang, L., Wei, L., He, L.X., et al.: A class of hybrid DG/FV methods for conservation laws II: two-dimensional cases[J]. *J. Comput. Phys.* **231**(4), 1104–1120 (2012)
15. Ii, S., Xiao, F.: CIP/multi-moment finite volume method for Euler equations: a semi-Lagrangian characteristic formulation[J]. *J. Comput. Phys.* **222**(2), 849–871 (2007)
16. Chen, C., Xiao, F.: Shallow water model on cubed-sphere by multi-moment finite volume method[J]. *J. Comput. Phys.* **227**(10), 5019–5044 (2008)
17. Xie, B., Deng, X., Sun, Z., et al.: A hybrid pressure–density-based Mach uniform algorithm for 2D Euler equations on unstructured grids by using multi-moment finite volume method[J]. *J. Comput. Phys.* **335**, 637–663 (2017)
18. Pan, L., Xu, K.: A compact third-order gas-kinetic scheme for compressible Euler and Navier–Stokes equations[J]. *Commun. Comput. Phys.* **18**(04), 985–1011 (2015)
19. Pan, L., Xu, K.: A third-order compact gas-kinetic scheme on unstructured meshes for compressible Navier–Stokes solutions[J]. *J. Comput. Phys.* **318**, 327–348 (2016)

20. Li L, Liu X, Lou J, Luo H, Nishikawa H, and Ren Y. "A discontinuous Galerkin method based on variational reconstruction for compressible flows on arbitrary grids". 56th AIAA Aerospace Sciences Meeting, AIAA Paper p. 0831, Kissimmee, Florida, (2018)
21. Li L, Liu X, Lou J, Luo H, Nishikawa H, and Ren Y. "A Finite Volume Method Based on Variational Reconstruction for Compressible Flows on Arbitrary Grids". 23rd AIAA Computational Fluid Dynamics Conference, AIAA Paper 2017–3097, Denver, Colorado, (2017)
22. Nishikawa H, An implicit gradient method for cell-centered finite-volume solver on unstructured grids. In: AIAA Scitech 2019 Forum, AIAA p. 1155 (2019)
23. Cheng, J., Liu, T.: A variational reconstructed discontinuous Galerkin method for the steady-state compressible flows on unstructured grids[J]. *J. Comput. Phys.* **380**, 65–87 (2019)
24. Liu, X., Xia, Y., Luo, H.: A reconstructed discontinuous Galerkin method for compressible turbulent flows on 3D curved grids[J]. *Comput. Fluids* **160**, 26–41 (2018)
25. Sethian, J.A.: Level set methods and fast marching methods: evolving interfaces in computational geometry, fluid mechanics, computer vision, and materials science[M]. Cambridge University Press, Cambridge (1999)
26. Gremaud, P.A., Kuster, C.M.: Computational study of fast methods for the eikonal equation[J]. *SIAM J. Sci. Comput.* **27**(6), 1803–1816 (2006)
27. Jiang, G.S., Peng, D.: Weighted ENO schemes for Hamilton-Jacobi equations[J]. *SIAM J. Sci. Comput.* **21**(6), 2126–2143 (2000)
28. Liu, X.D., Osher, S., Chan, T.: Weighted essentially non-oscillatory schemes[J]. *J. Comput. Phys.* **115**(1), 200–212 (1994)
29. Shu, C.W., Osher, S.: High-order essentially nonoscillatory schemes for Hamilton-Jacobi equations[J]. *SIAM J. Numer. Anal.* **28**(4), 907–922 (1991)
30. Zhang, Y.T., Zhao, H.K., Qian, J.: High order fast sweeping methods for static Hamilton-Jacobi equations[J]. *J. Sci. Comput.* **29**(1), 25–56 (2006)
31. Li, F., Shu, C.W., Zhang, Y.T., et al.: A second order discontinuous Galerkin fast sweeping method for eikonal equations[J]. *J. Comput. Phys.* **227**(17), 8191–8208 (2008)
32. Zhang, Y.T., Chen, S., Li, F., et al.: Uniformly accurate discontinuous Galerkin fast sweeping methods for eikonal equations[J]. *SIAM J. Sci. Comput.* **33**(4), 1873–1896 (2011)
33. Cheng, Y., Wang, Z.: A new discontinuous Galerkin finite element method for directly solving the Hamilton-Jacobi equations[J]. *J. Comput. Phys.* **268**, 134–153 (2014)
34. Luo, S.: A uniformly second order fast sweeping method for eikonal equations[J]. *J. Comput. Phys.* **241**, 104–117 (2013)
35. Zhao, H.: Parallel implementations of the fast sweeping method[J]. *J. Comput. Math.* **25**(4), 421–429 (2007)
36. Detrixhe, M., Gibou, F., Min, C.: A parallel fast sweeping method for the eikonal equation[J]. *J. Comput. Phys.* **237**(1), 46–55 (2013)
37. Yang, J., Stern, F.: A highly scalable massively parallel fast marching method for the eikonal equation[J]. *J. Comput. Phys.* **332**, 333–362 (2017)
38. Fares, E., Schröder, W.: A differential equation for approximate wall distance[J]. *Int. J. Numer. Meth. Fluids* **39**(8), 743–762 (2002)
39. Zhou C, Wang Z J. 53rd AIAA Aerospace Sciences Meeting - CPR High-order Discretization of the RANS Equations with the SA Model[C]. In: AIAA Aerospace Sciences Meeting, (2015)
40. Schoenawa, S., Hartmann, R.: Discontinuous Galerkin discretization of the Reynolds-averaged Navier-Stokes equations with the shear-stress transport model[J]. *J. Comput. Phys.* **262**, 194–216 (2014)
41. Xia, H., Tucker, P.G.: Finite volume distance field and its application to medial axis transforms[J]. *Int. J. Numer. Meth. Eng.* **82**(1), 114–134 (2010)
42. Castro, M., Gallardo, J.M., Parés, C.: High order finite volume schemes based on reconstruction of states for solving hyperbolic systems with nonconservative products. Applications to shallow-water systems[J]. *Math. Comput.* **75**(255), 1103–1134 (2006)
43. Parés, C.: Numerical methods for nonconservative hyperbolic systems: a theoretical framework[J]. *SIAM J. Numer. Anal.* **44**(1), 300–321 (2006)
44. Castro, M., Pardo, A., Parés, C., Toro, E.F.: On some fast well-balanced first order solvers for nonconservative systems[J]. *Math. Comput.* **79**(271), 1427–1472 (2010)
45. Dumbser, M., Toro, E.F.: A simple extension of the Osher Riemann solver to non-conservative hyperbolic systems[J]. *J. Sci. Comput.* **48**(1–3), 70–88 (2011)
46. Dumbser, M., Balsara, D.S.: A new efficient formulation of the HLLEM Riemann solver for general conservative and non-conservative hyperbolic systems[J]. *J. Comput. Phys.* **304**, 275–319 (2016)

47. Dal Maso, G., LeFloch, P.G., Murat, F.: Definition and weak stability of nonconservative products[J]. *J. De Mathématiques Pures Et Appliquées* **74**(6), 483–548 (1995)
48. Xu, J.L., Yan, C., Fan, J.J.: Computations of wall distances by solving a transport equation[J]. *Appl. Math. Mech.* **32**(2), 141–150 (2011)
49. Luo, H., Baum, J.D., Löhner, R.: A discontinuous Galerkin method based on a Taylor basis for the compressible flows on arbitrary grids[J]. *J. Comput. Phys.* **227**(20), 8875–8893 (2008)
50. Li, W.A., Ren, Y.X.: High-order k-exact WENO finite volume schemes for solving gas dynamic Euler equations on unstructured grids[J]. *Int. J. Numer. Methods Fluids* **70**(6), 742–763 (2012)
51. Shu, C.W., Osher, S.: Efficient implementation of essentially non-oscillatory shock capturing schemes. *J. Comput. Phys.* **77**(2), 439–471 (1988)
52. Wang, Q.J., Ren, Y.X., Sun, Z.S., Sun, Y.T.: Low dispersion finite volume scheme based on reconstruction with minimized dispersion and controllable dissipation. *Sci. China Phys. Mech. Astron.* **56**(2), 423–431 (2013)
53. Wang, Q.J., Ren, Y.X.: An accurate and robust finite volume scheme based on the spline interpolation for solving the Euler and Navier-Stokes equations on non-uniform curvilinear grids[J]. *J. Comput. Phys.* **284**, 648–667 (2015)
54. Zalesak, S.T.: Fully multidimensional flux-corrected transport algorithms for fluids[J]. *J. Comput. Phys.* **31**(3), 335–362 (1979)
55. LeVeque, R.J.: High-resolution conservative algorithms for advection in incompressible flow[J]. *Siam J. Numer. Anal.* **33**(2), 627–665 (1996)

**Publisher's Note** Springer Nature remains neutral with regard to jurisdictional claims in published maps and institutional affiliations.